Universidade de Aveiro
2015

Departamento de Química

RAQUEL TEIXEIRA SABORANO

METABOLOMIC STUDY OF CELLULAR RESPONSES TO SILK NANOPARTICLES

ESTUDO METABOLÓMICO DAS RESPOSTAS CELULARES A NANOPARTÍCULAS DE SEDA

Universidade de Aveiro **Departamento de Química**
2015

RAQUEL TEIXEIRA SABORANO

METABOLOMIC STUDY OF CELLULAR RESPONSES TO SILK NANOPARTICLES

ESTUDO METABOLÓMICO DAS RESPOSTAS CELULARES A NANOPARTÍCULAS DE SEDA

Dissertation submitted to the University of Aveiro to fulfil the requirements for the degree of Master in the field of Clinical Biochemistry, done under the scientific supervision of Dr Iola Melissa Fernandes Duarte, Principal Investigator at CICECO – Aveiro Institute of Materials, Department of Chemistry of the University of Aveiro and Dr Philipp Seib, Principal Investigator at the Strathclyde Institute of Pharmacy and Biomedical Sciences of the University of Strathclyde, Glasgow, United Kingdom.

This work was developed in the scope of the project CICECO-Aveiro Institute of Materials (Ref. FCT UID/CTM/50011/2013), financed by national funds through the FCT/MEC and when applicable co-financed by FEDER under the PT2020 Partnership Agreement. The Portuguese National NMR (PTNMR) Network, supported with FCT funds, and funding from the University of Strathclyde (Grant ref. 12101 DD1720 RDF) are acknowledged.

Home is where the heart is.

Examining Committee

President

Prof. Pedro Miguel Dimas Neves Domingues
Auxiliary Professor with Aggregation, University of Aveiro

Prof. Brian James Goodfellow
Auxiliary Professor, University of Aveiro

Dr. Iola Melissa Fernandes Duarte
Principal Investigator, University of Aveiro

Acknowledgements

This stage was over in the blink of an eye! At this moment I can only thank everyone who accompanied me, who made every day better than the last, who showed me that there is nothing better than friendship and who made me feel at home during these wonderful five years in Aveiro.

In the first place, I would like to thank my supervisors. To Dr. Iola Duarte, I would like to thank for all the hours spent teaching me, exchanging ideas, supporting me and, above all, the sympathy with which you always welcomed me. Thank you for giving me the opportunity to carry out this work. To Dr. Philipp Seib, I would like to express my sincere gratitude for the shared knowledge, the help and the availability that you always showed to me.

I would like to specially acknowledge Joana Carrola. For all the support throughout this year, for all the questions answered, for the company and for the moments of laughter in the laboratory. To Ivana, Sérgio, Leandro and Lisa, thank you for doing that workplace so enjoyable to share with you.

To the University of Aveiro and the Chemistry Department, which in this huge universe made me come across with some of the best people I've ever met. To Di, the one who brought me to this family that constitutes NEQ and to all the people who were part of it. To you, my dear friends, who have always been here: Mélanie, Maria, Sofia, Bebiana, Vanessa, Madalena, Diana and Adriana, Calixto and Samuel. To you Ana Alves, that became such a great friend and, although far, will always be close.

In particular, to you Margarida. You, who made my days better, who joined me in the discovery of new places, who allow me to teach and learn, who gave the word friendship another meaning, who understood so many things even if I didn't say anything. I also thank you for the strength and support you always gave me, and for believing in me even when I couldn't.

To you, who always knew how to put a smile on my face, who believed that a friendship like ours could only grow bigger every day that goes by, that supported me like no one else this entire year. Thank you Vasco, for your patience and for bringing me peace and happiness, every single day.

Finally, to my family that has always been by my side, but especially to my parents. To you, who always allowed me to pursuit my dreams, who always believed in me and supported my decisions, who taught me to be strong and fight for what I believe, who are my role models, who are the best people I could ever have by my side. A truthful thank you, for your presence and patience, but above all for helping me making this possible.

Palavras-chave

Nanopartículas de seda; Metabolómica; Nanomedicina; Nanofármacos; Espectroscopia de Ressonância Magnética Nuclear (RMN); Nanotoxicologia.

Resumo

A aplicação da metabolómica com o intuito de revelar biomarcadores de eficácia ou toxicidade, assim como de fornecer uma compreensão bioquímica de mecanismos de ação, tem ganho maior interesse na comunidade científica. Neste trabalho os efeitos das nanopartículas de seda no metabolismo de macrófagos, que são um tipo celular importante no que diz respeito à incorporação de nanopartículas, foram investigados por metabolómica de espectroscopia de Ressonância Magnética Nuclear (RMN). Inicialmente, espectroscopia de RMN 1D e 2D foi aplicada para determinar a composição metabólica de macrófagos de rato (linha celular RAW 264.7), através da análise de extratos aquosos e lipídicos. Cerca de quarenta metabolitos foram identificados, estabelecendo uma base de dados dos metabolitos de macrófagos de rato. De seguida, esses macrófagos foram expostos a duas concentrações de nanopartículas de seda (10 e 500 µg/mL), selecionadas com base nos dados citotoxicológicos recolhidos previamente a este trabalho, e o seu impacto no metabolismo foi averiguado usando a mesma metodologia. Análise multivariada foi aplicada aos espectros de ^{1}H RMN 1D de forma a investigar as alterações na composição dos macrófagos durante a exposição às nanopartículas de seda (SNPs). A concentração baixa de SNPs induziu poucas alterações no metaboloma celular comparativamente à concentração alta de SNPs, que resultou em alterações bioquímicas no metabolismo energético e ciclo do ácido cítrico, distúrbios no metabolismo de aminoácidos e modificações na membrana celular. Algumas variações foram comuns a todos os períodos de exposição, tais como o aumento dos aminoácidos de cadeia ramificada, lactato e tirosina, e a diminuição de glutamina, taurina, myo-inositol e ATP/ADP, enquanto que outras se revelaram ser mais específicas em relação ao tempo de exposição. As flutuações dependentes do tempo foram também visíveis nos lípidos, onde o colesterol, ésteres de colesterol e esfingomielina se encontraram mais elevados nas amostras expostas à concentração elevada de SNPs, enquanto que os ácidos gordos insaturados, plasmalogénio e fosfatidilcolina estavam mais elevados nos controlos.

Estes resultados demonstraram que a aplicação de metabolómica de RMN para avaliar o desempenho de nanofármacos pode ser uma ferramenta importante para melhorar a nossa compreensão das interações célula-nanomaterial e os mecanismos subjacentes à toxicidade observada.

Keywords

Silk nanoparticles; Metabolomics; Nanomedicine; Nanopharmaceuticals; Nuclear Magnetic Resonance spectroscopy; Nanotoxicology.

Abstract

The use of metabolomics to reveal response markers of efficacy or toxicity, as well as to provide biochemical insight into mechanisms of action has gained increasing interest in the research community. In this work, the effects of silk nanoparticles on the metabolism of macrophages, which are an important cell type in regard to NP uptake, was addressed through Nuclear Magnetic Resonance (NMR) spectroscopy metabolomics. Firstly, 1D and 2D NMR spectroscopy was applied to determine the metabolic composition of murine macrophages (RAW 264.7 cell line), through the analysis of both aqueous and lipid extracts. Almost forty metabolites were identified, establishing a database of metabolites of murine macrophages. Afterwards, murine macrophages were exposed to two concentrations of silk nanoparticles (10 and 500 µg/mL), selected based on cytotoxicity data collected previously to this work, and the impact on their metabolic composition was assessed. Multivariate analysis was applied to the 1D ^{1}H NMR spectra in order to search the compositional changes in macrophages during silk nanoparticles' (SNPs) exposure. It was found that the low concentration SNPs induced few changes in the cells metabolome compared to the high concentration SNPs, which resulted in biochemical changes related to energy metabolism and TCA cycle, disturbance of amino acids metabolism and cell membrane modification. Some variations were common to all exposure periods, such as the increase in branched chain amino acids, lactate and tyrosine and the decrease in glutamine, taurine, myo-inositol and ATP/ADP, whereas other variations seemed to be more time-specific. The time-dependent fluctuations were also visible in lipids, where cholesterol, cholesterol esters and sphingomyelin were found to be relatively higher in SNP-exposed samples, while unsaturated fatty acids, plasmalogen and phosphatidylcholine were higher in controls.

These results have shown that the use of NMR metabolomics to evaluate a nanomedicine performance may be a powerful tool to improve our understanding of cell-nanomaterial interactions and of the mechanisms underlying observed toxicities.

Contents

Abbreviations and Acronyms

16-HBE	Human bronchial epithelial cells
A549	Adenocarcinomic human alveolar basal epithelial cells
ADME	Absorption, distribution, metabolism and excretion
ADP	Adenosine diphosphate
AFM	Atomic force microscopy
ANOVA	Analysis of variance
ATP	Adenosine triphosphate
BCAA	Branched chain amino acids
Cho	Choline
Chol	Cholesterol
CI	Confidence interval
CLSM	Confocal laser scanning microscopy
COSY	Correlation spectroscopy
CPMG	Carr – Purcell – Meiboom – Gill
Cr	Creatine
d	Effect size
DNA	Deoxyribonucleic acid
EPR	Enhanced permeability and retention
FA	Fatty acids
FDA	Food and Drug Administration
FID	Free Induction Decay
FITC	Fluorescence isothiocyanate
GC	Gas chromatography
GSH	Glutathione reduced
GSSG	Glutathione oxidized
HaCat	Spontaneously immortalized, human keratinocyte line
HCA	Hierarchical Cluster Analysis
HDL	High-density lipoprotein

HeLa	Henrietta Lacks' cells
HGF	Human gingival fibroblast cells
HPLC	High-performance liquid chromatography
HRMAS	High Resolution Magic Angle Spinning
HSQC	Heteronuclear single quantum correlation
i.m.	Intra-muscular
i.t.	Intra-tumoral
i.v.	Intravenous
IC50	Half maximal inhibitory concentration
IL	Interleukin
Ig	Immunoglobulin
JRES	J-resolved spectroscopy
KC	Kupffer cells
Lb	Line broadening
LC	Liquid chromatography
LDL	Low-density lipoprotein
LPC	Lysophosphatidylcholine
LPE	Lysophosphatidylethanolamine
LV	Latent variables
m-ino	*myo*-inositol
MPS	Mononuclear phagocyte system
MRC-5	Human Fetal Lung Fibroblast Cells
MRI	Magnetic resonance imaging
MS	Mass spectrometry
MTT	(3-(4, 5-Dimethylthiazol-2-yl)-2, 5-Diphenyltetrazolium Bromide)
MVA	Multivariate Analysis
NAD	Nicotinamide adenine dinucleotide
NMR	Nuclear Magnetic Resonance

NO	Nitric oxide
NOESY	Nuclear Overhauser effect spectroscopy
NP	Nanoparticle
NR	Nanorods
PCA	Principal Component Analysis
PCho	Phosphocholine
PCr	Phosphocreatine
PEG	Polyethylene glycol
PK	Pharmacokinetic
PLGA	Poly (D, L – Lactic-co-glycolic acid)
PLS-DA	Partial Least Squares Discriminant Analysis
PTC	Phosphatidylcholine
PTE	Phosphatidylethanolamine
QTOF	Quadrupole time-of-flight
RAW 264.7	Mouse leukemic monocyte macrophage cell line
RNA	Ribonucleic acid
ROS	Reactive Oxygen Species
SEM-EDS	Scanning Electron Microscope and Energy Dispersive X-Ray Spectrometer
SM	Sphingomyelin
SNP	Silk nanoparticle
SOP	Standard operating procedure
TCA	Tricarboxylic acid cycle
TEM	Transmission electron microscopy
siRNA	Small interfering RNA
TG	Triglycerides
TMS	Tetramethylsilane
TNF-α	Tumor necrosis factor alpha
TOCSY	Total correlation spectroscopy

UDP	Uridine diphosphate
UFA	Unsaturated fatty acid
Un	Unassigned
UPLC	Ultra Performance Liquid Chromatography
USPIO	Ultra-small superparamagnetic particles of iron oxides
UTP	Uridine trphosphate
UV	Unit Variance
V_d	Volume of distribution
VEDIC	Video-Enhanced Differential Interference Contrast
VIP	Variable importance in the projection
VLDL	Very-low-density lipoprotein
WET	Water suppression enhanced through T1 effect

CHAPTER 1 - Introduction

1.1. Introducing nanomedicine

1.1.1. General overview

Nowadays, the application of nanomaterials to therapy and diagnostic ends is one of the fastest growing areas in nanotechnology *(1,2)*. Nanomedicine is a field of science which aims at improving diagnosis and treatment of life-threatening and debilitating diseases for which there are currently no adequate therapies *(1–3)*. The definition of nanomedicine was achieved via consensus conference by the European Science Foundation's (ESF) Forward Look Nanomedicine in the following way: "Nanomedicine is the science and technology of diagnosing, treating and preventing disease and traumatic injury, of relieving pain, and of preserving and improving human health, using molecular tools and molecular knowledge of the human body."*(4)*

The main areas of research and development of nanomedicine being developed for healthcare applications encompass *(1,2)*:

a) Diagnostics, devices/biosensors, and surgical tools used outside the patient;
b) Nanostructured biomaterials (often combined with cell therapy) for biomedical applications, such as oral, parental, pulmonary, surgical implantation, or tissue regeneration;
c) Nanopharmaceuticals (nanomedicines) and nanoimaging agents for patient administration, with diagnostic or therapy purposes.

Nanomedicines are nanometre size scale complex systems, consisting of at least two components, one of which is the active ingredient, and being developed either as drug delivery systems or biologically active drug products. They are carefully engineered with innovative methodologies for physicochemical and biological characterization to ensure optimization of properties relevant to the clinical setting *(5,6)*.

Nanomaterials used as drug delivery systems or imaging agents are generally below 100 nm in size in at least one dimension and may be constructed from a wide range of organic and inorganic materials. They include liposomal and lipidic complexes, antibody-based drug conjugates, polymer therapeutics, and nanoparticles. Figure 1 schematically shows these and other classes of nanomedicines. Each nano-sized construct can have different dimensions and a different surface composition, each class of nanomedicines displaying typical size ranges in the nanoscale *(1,3)*.

The first drug delivery systems are now called 1st generation nanomedicines, and have already entered routine clinical use.

There are several reasons for the rational design and development of nanomedicines: they can potentially improve transport of drugs across both external biological barriers (e.g. gastrointestinal (GI) tract and lung) or internal barriers (e.g. blood brain barrier); improve drug solubilisation and protection from metabolism; improve disease-specific targeting and/or controlled release *(1–3)*. The encapsulation of drugs can also protect them against degradation by the body's defence system, thus providing stability in systemic circulation. Nanocarriers may release drugs with varying kinetics, based on their ability to respond to physically stimuli (e.g. temperature, electric or magnetic field, light and ultrasounds), chemical stimuli (pH, ionic, and redox status), or biological stimuli (e.g. enzymes and inflammation). This provides an additional tool for controlling release kinetics besides diffusion and matrix degradation. Thus, the need of combining enhanced site specificity and local controlled release of the bioactive agent has encouraged the development of nanoparticles as nanomedicines *(7,8)*.

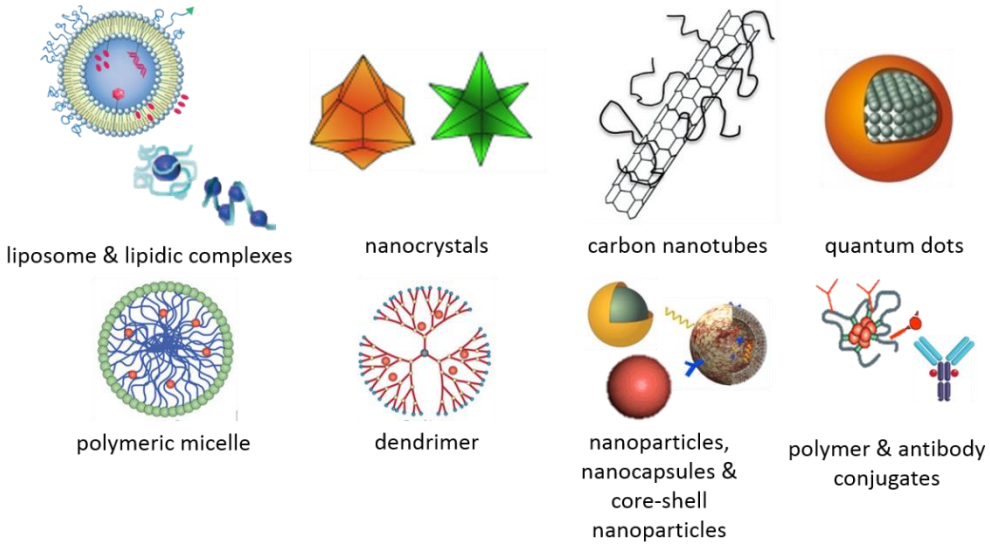

Figure 1 - Schematic representation of different nanomedicines under development. The nanomedicines models are not drawn to scale. Based on *(2)*.

Encapsulating active ingredients into nanocarriers has allowed maximising therapeutic efficacy and patient convenience, because the pharmacokinetic (PK) profile could be improved compared to small molecule drugs. While small drugs distribute evenly throughout the body, resulting in a large volume of distribution (V_d), nanocarriers can take advantage of the enhanced permeability and retention (EPR) effect of leaky vasculature often observed in

tumour and inflamed tissue. Tumour vasculature is typically comprised of poorly aligned endothelial cells with wide fenestrations (larger than 100 nm in size), and tumour tissue lacks functional lymphatics, resulting in preferred accumulation of nanocarriers in these tissues over healthy ones. Thus, the EPR effect leads to altered biodistribution, where the nano-sized drug shows selective tumour accumulation thereby reducing V_d and improving target specificity of the treatment. Hence, the combination of reduced toxicity and superior therapeutic effect greatly improves the therapeutic window *(9,10)*.

An additional advantage of using nanocarriers is the possibility to achieve active targeting by attaching specific ligands to their surface, which interact with complementary cell receptors known to be overexpressed at the target tissue. The envisaged result is increased efficacy and reduced systemic toxicity due to accelerated clearance by the mononuclear phagocyte system (MPS) *(3)*. Furthermore, while small molecular weight drugs can normally access the cell by diffusion across the plasma membrane and be effectively effluxed, the endocytic uptake of NPs can overcome drug resistance mechanisms *(10)*.

The recognition and uptake of nanoparticles by the body can be made by non-phagocytic eukaryotic cells, macrophages and dendritic cells. When the body recognizes NPs as foreign substances, the reticulum-endothelial system – now called the mononuclear phagocyte system (MPS) –, eliminates them from the bloodstream and the uptake occurs in the liver or the spleen. Moreover, opsonisation of the NPs may also occur in the bloodstream, in order to make the foreign substance visible to macrophages. In this way, particles attach to the macrophage surface through specific receptor-ligand interactions. To overcome these limitations, surface modifications such as altering the NP charge permits targeting and selective cellular binding *(11,12)*.

Currently, modern nanomedicines fit into three groups of emerging nanotechnologies: the first group consists of 1st generation nanomedicines that already entered routine clinical use (Table I). The second group encompasses nanomedicines being proposed for or currently undergoing clinical development for treating several diseases, manly cancer, and their clinical safety and efficacy status are already beginning to emerge. Finally, the third group includes putative nanomedicines based on novel nanomaterials: fullerenes, and carbon nanotubes, inorganic nanoparticles (e.g. gold, silver, quantum dots, silica and core shell silica-based nanoparticles), and natural and synthetic polymer-based nanoparticles, nanocapsules, and other sell-assembling nanostructures, and complex nano-architectures

manufactured via new routes by innovative methods *(1,2)*. Of these, only few are near to realising a clinical candidate and exhaustive pre-clinical testing is still needed.

Table I – Main classes of nanomedicines already in the market or under clinical development, adapted from *(1)*.

	CLASS	*TYPICAL SIZE (NM)*	*TYPICAL ADMINISTRATION ROUTE*	*USE*	*PRODUCT EXAMPLES*
PRODUCTS APPROVED FOR THE MARKET	Coated iron colloidals	10-100	i.v. (intravenous)	Anaemia MRI imaging agents	Feridex, Venofer
	Liposomes and lipidic drug carriers	60-80 nm - > 1 μM aggregates	i.v.	Cancer Opportunistic infections	Doxil/Caelix Ambissome, Ablecet
	Drug nanocrystals	50–1000	oral	Immunosuppressive Anti-emetic	Rapamune, Emend
	Antibody targeted radiotherapy	< 20	i.v.	Cancer	Zevalin, Bexxar
	Antibody-drug conjugate	< 20	i.v.	Cancer	Adcetris, Kadcyla
	Nanoparticles		i.v.	Cancer	Abraxame
	Polymer therapeutics ➢ Polymeric drugs and sequestrants	NA	i.m. (intramuscular), oral	Multiple sclerosis Renal failure, diabetes	Copaxone´ Renagel, Welchol
	➢ Polymer protein conjugates	10-20		Cancer, infectious diseases	Neulasta, PEGasys
PRODUCTS IN CLINICAL DEVELOPMENT	Polymer therapeutics ➢ Polymeric-drugs conjugates	5-20	i.v., oral	Cancer	Opaxio, Prolindac NK150, SP1049
	➢ Block co-polymer micelles	20-100	i.v.	Cancer siRNA delivery	
	➢ Sell assembled polymer conjugate nanoparticles	70	i.v.		CALAA01
	Liposomal combination therapy		i.v.	Cancer	CPX-351
	Hollow gold nanoparticles	150	i.v.	Cancer	Aurolase
	Silica nanoparticles		i.v	Cancer	
	Iron oxide nanoparticles		i.t. (intra-tumoral)	Cancer (thermal ablation)	Nanoderm
	Silver nanoparticles		topical	Anticancer/ Dermatitis	Nucryst
	Hafnium oxide crystals		i.t.	Cancer (radiotherapy)	NBTXR3

1.1.2. Silk nanoparticles as emerging nanomedicines

Silk is a biologically derived protein-based fibre-forming material spun by some *Arachnida* and *Lepidoptera larvae* such as silkworms, spiders, scorpion, mites and flies *(13,14)*. Natural silk fibre consists of two types of proteins: silk fibroin (commonly referred as silk) and sericins. Sericins in association with silk fibroin have been shown to cause an inflammatory response, due to upregulated immunoglobulins (IgEs), thus they are usually removed for medical applications *(15)*. One of the most common forms of silk is obtained from the silkworm *Bombyx mori*, with typical molecular weights between 200 and 400 kDa. In fact, *B. mori* silk is the most commonly used in biomedical applications, including drug delivery, as compared to spider, since they are easier to domesticate and to harvest silk. In general, to prepare *B. mori* silk, the cocoons are boiled in an aqueous alkaline solution (most commonly sodium carbonate) to remove sericin from the silk fibroin (degumming) and the native protein is then fragmented, leading to a lower molecular weight silk *(16,17)*. Silk fibroin contains large internal repeats, the amino acid composition of which consists of a sequence of six residues $(Gly\text{-}Ala\text{-}Gly\text{-}Ala\text{-}Gly\text{-}Ser)_n$, which lead to the formation of rigid anti-parallel β-sheet structures due to the dominance of hydrophobic domains. These structures confer the strength, flexibility and resiliency associated to silk fibres *(14,18)*.

The ancient use of silk as a suture material, together with its known minimal adverse effects, has led to the recent approval of this fibre for medical applications by the Food and Drug Administration (FDA), for example as a surgical mesh *(16)*. Also, silk fibres are considered promising materials for other biomedical applications, including drug delivery, due to their good biocompatibility, slow degradability and versatility to generate various materials formats such as films, gels, fibres, scaffolds and micro- or nanoparticles *(13,19)*. Additionally, silk is less inflammatory than other common biodegradable polymers such as poly(lactide) *(13,16)*.

One of the advantages of silk, that makes it potentially suitable for drug-delivery applications, is that it is typically processed into an aqueous solution (referred to as regenerated silk) by disrupting the hydrogen bonding of the degummed silk fibres through the use of chaotropic agents and elevated temperatures (Figure 2) *(10,14,20)*. These mild processing conditions, without the use of organic solvents or harsh environmental conditions and chemical modifications, favour the development of silk beyond its traditional use as a suture material. Several different material morphologies can be formed from natural silk

fibre for utilization in biomaterials. Regenerated silk fibroin solution can be processed into porous silk sponges, silk films, micro- or nanoscale coatings, hydrogels and micro- and nanoparticles *(14,19)*. Additionally, the material properties of silk fibroin biomaterials can be tightly controlled during processing and fabrication, resulting in a broad range of silk-based systems available for medical applications *(16)*.

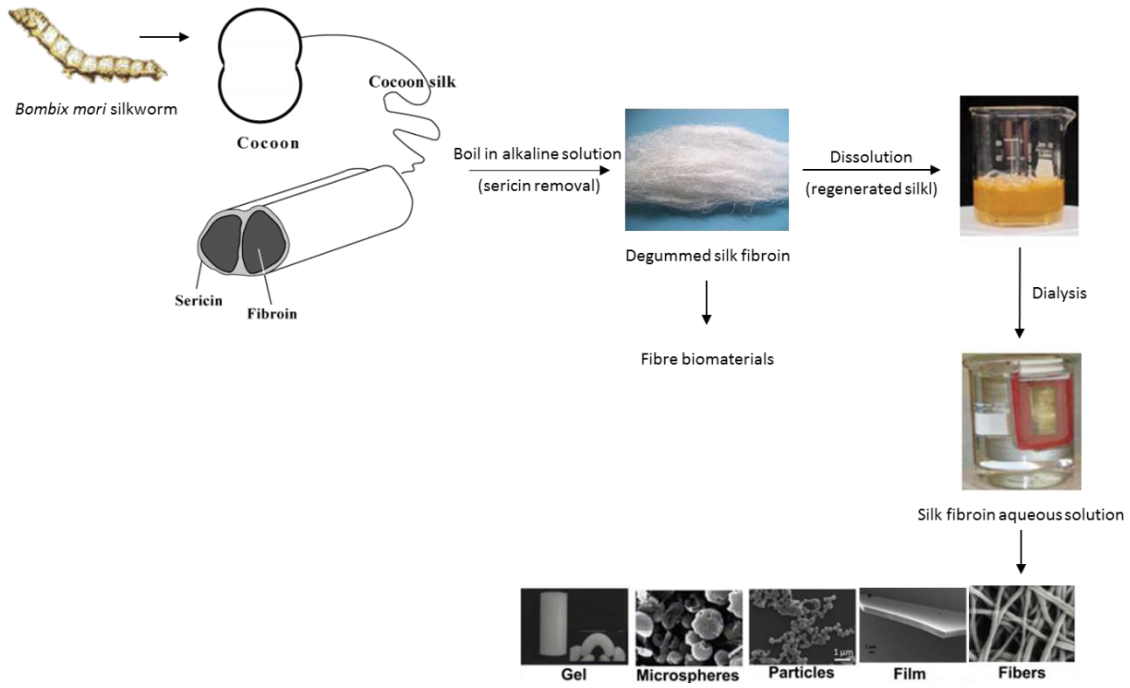

Figure 2 - Silk fibroin preparation. *Bombyx mori* cocoons are purified from sericin by means of boiling in an alkaline solution. Degummed silk fibroin can be processed into fibre biomaterials including sutures, meshes, woven fabrics, yarns and ropes. To prepare aqueous silk solution, degummed silk fibroin is dissolved in salt and then the salt is removed with dialysis. The aqueous silk solution can then be processed into various material formats for drug delivery. Adapted from *(16)*.

As for other natural polymers, an additional advantageous aspect of silk is that it may be metabolized *in vivo* by digestive enzymes into peptides and amino acids *(13)*. Indeed, even though silk degradation and excretion from the body remain to be established, enzymatic degradation, as part of the foreign body response, and further clearance by macrophages, appear to be the most viable route for *in vivo* biodegradation *(10)*. The rate and behaviour of the degradation of silk by proteases is dependent on many factors, including silk processing and material properties (morphology, molecular mass and crystallinity/β-sheet content), and mechanical and biological conditions at the site of implantation *(14,16)*. Several types of proteases are being studied, including α-chymotrypsin and collagenases, which catalyse

hydrolysis reactions and contribute to silk biodegradation in peptide fragments and amino acids that can be readily metabolized and excreted *(14)*. While chymotrypsin is a mammalian enzyme, synthesized in the pancreas and excreted from there, and consequently accumulated in the duodenum of the gastrointestinal tract, protease type XIV is not. Thus, protease XIV does not reflect degradation properties *in vivo*, which need to be determined empirically. Both enzymes have been used to compare the degradation properties and to understand the enzymatic degradation kinetic of different silk formulations, but only the first one is able to reflect the *in vivo* behaviour and overall tolerance *(20,21)*.

A few studies have examined the ability of silk to entrap and release (model) drugs, showing that silk-based biomaterials are able to stabilize the payload and control drug release using endogenous parameters such as crystallinity and molecular weight of the silk fibroin. Drugs are typically incorporated by mixing the drug with the silk solution either before material production or after the formation of the drug delivery system (by surface decoration with the drug or by means of either chemical coupling or adsorption). Native silk has the ability to strongly absorb low molecular weight drugs, the overall loading efficiency being dependent on the drug net charge and its correlation with silk's isoelectric point *(10,16)*. The release characteristics have been found to be governed either by diffusion of the payload from the carrier or by solubilisation and/or degradation of the silk. For example, when casting a thin silk film, the dried fibroin (also referred as silk I) was found to be completely water soluble and, therefore, the drug payload was released in accordance with the solubilisation characteristics of the film in aqueous environment *(10)*. Silk I could also be easily converted into a stabilized silk II form (richer in β–sheets) through a gentle process where water is removed from the hydrophobic domains, permitting tight packing of these β–sheets *(14,20)*. Importantly, the manipulation of silk crystallinity has been found to provide control over the release of doxorubicin (a clinically relevant chemotherapeutic agent), thus potentially allowing systemic and local adverse effects to be minimised while maximising therapeutic efficacy *(21)*. Moreover, inducing crystallinity in silk makes it more compatible with a wide range of payloads, including proteins *(22)*.

Several silk formats have already been tested as drug delivery systems, taking into account the multitude of factors that govern the final design of the system *(10)*. Silk films have been used for promoting long-term adenosine release from adenosine kinase deficient embryonic stem cells. This study has demonstrated that silk fibroin constitutes a suitable

material for the directed differentiation of embryonic stem cells and for cell-mediated therapeutic release of adenosine. Therefore, silk films decorated with bioactive molecules could be used for local drug delivery via direct implantation *(15)*. Also, Seib's team revealed that doxorubicin-loaded silk films could directly be applied to mice using a humanised orthotropic breast cancer model (adenocarcinoma). By manipulating silk mechanical properties, the release of doxorubicin could be controlled, which minimised systemic and local adverse effects, while maximising therapeutic impact *(21)*.

Regarding silk hydrogels, they have been combined with osteoblasts-like cells and injected in critical-size femur defects in rabbits. This resulted in greater trabecular bone volume and thickness, with significant higher mineral and rate of bone formation *(14)*. In another study, self-assembling silk hydrogels were loaded with doxorubicin and further injected in tumours of mice. Reducing primary tumour growth and metastatic spread, silk hydrogels were found to be well suited for the local delivery of chemotherapy of breast cancer *(22)*.

In the case of silk microspheres, when they were loaded with horseradish peroxidase (HRP), a model drug, they showed controlled and sustained release of action for 10 to 15 days *(23)*. Moreover, a silk/polymeric scaffold system also showed high encapsulation efficiencies and good control over the feature sizes which allowed a slow release of Bone Morphogenetic Proteins (BMPs) during 14 days *(15)*.

Silk nanoparticles (SNPs) are also being designed as new drug nanocarriers. Nanoparticles provide advantages over the administration of free drugs and other silk-based biomaterials since they can overcome drug resistance mechanisms, decrease side-effects, enhance drug bioavailability and have a higher intracellular uptake compared to microparticles, for example. Moreover, they can be easily transported via the circulation to various body sites, thus improving medical treatments *(10,18)*. Some studies involving silk nanoparticles as drug delivery systems were performed. Zhao's team has investigated the controlled release properties of SNPs containing indomethacin (a non-steroidal anti-inflammatory drug). It was demonstrated that SNPs may sustain the indomethacin release and these nanoparticles can be used effectively as a drug carrier *(18)*. SNPs were also tested in the cytosol of murine squamous cell carcinoma cells. The growth factor release from the nanoparticles showed significantly sustained release over 3 weeks, implying potential

application as a growth factor delivery system, without significant changes regarding toxicity *(24)*.

Additionally, SNPs were also prepared for anticancer drug delivery. Using magnetic SNPs loaded with doxorubicin, Tian *et al.* studied the magnetic-guided drug delivery in a humanized orthotropic breast cancer model and chemotherapy performance of drug-resistant cancer. These SNPs have demonstrated the ability of magnetic targeting *in vivo* and effective chemotherapy, working well as a novel drug delivery system in cancer therapy *(25)*. In another study, biological derived-silk based nanoparticles containing curcumin showed a higher efficiency against breast cancer cells and have potential to treat in-vivo breast tumours by local, sustained, and long-term therapeutic delivery *(26)*. For focal therapy of breast cancer, Seib *et al*. demonstrated the potential of silk to serve as a stimulus-responsive nanomedicine, with overall negative surface charge and pH-dependent release. Hence, SNPs loaded with doxorubicin were able to serve as a lysosomotropic delivery platform and overcome drug-resistance mechanisms *in vitro (19)*. In addition, the pH-sensitivity of the nanoparticles is effective for drug delivery systems application because of the difference between the extracellular pH of normal tissue (pH 7.2-7.4) and of many solid tumours (pH 6.2-6.9) *(7)*.

In parallel with the development of nanoparticles from *Bombix mori* silk, recombinant spider silks have been engineered for use in non-viral gene and siRNA delivery. Silk sequence was modified to control self-assembling of β-sheets structures in silk, but also cell-binding domains were included to enhance cell adhesion. The most widely studied spider silk in terms of variants is dragline silk from the spider *Nephila clavipes*. These recombinant silk-like polymers can be tailored to further control targeting, size, stability and related needs for gene delivery. In these studies, silk was prepared in the form of microcapsules, microspheres and polyioncomplexes *(15)*.

1.2. Safety issues and toxicity assessment of emerging nanomedicines

1.2.1. General remarks

For emerging nanomedicines, inspired on 1st generation products or based on novel nanomaterials, to progress towards clinical application, they must undergo a rigorous safety assessment, in order to estimate the risk-benefit in relation to a specific proposed clinical use. For that purpose, it is essential to establish the toxicity profile of each nanomedicine being developed, as well as to understand its mode of action and how its physicochemical properties influence both toxicity and efficacy *(1,2)*.

This task is often complicated, especially given that many variables may modulate the biological responses, including the size and surface chemistry of the nanoconstruct, the nature of the bioactive payload, the linking chemistry used between components, or the degradation of particular components into secondary products *(1,27)*. Whereas size and shape play a role in how the materials are distributed and eliminated of the body, affecting the mode of endocytosis, cellular uptake and the efficiency of particle processing in metabolic pathways, chemical composition at the surface of nanomedicines will mostly define their chemical interactions, because the surface is in direct contact with the body membranes *(27)*. Generally, the pharmacokinetics, body distribution, nanomedicine stability, and the metabolic fate of all components impact on the overall toxicological profile observed *(1)*.

Therefore, it is very important that the toxicological profile of a nanomedicine is evaluated in its entirety. However, at early development stages, the preliminary safety assessment of individual components (envisaged for incorporation into a nanomedicine) may also play a critical role in the design of the overall construct *(1,2)*. Figure 3 summarizes some of the tests that are typically used to assess the safety of component nanomaterials or the whole nanomedicine.

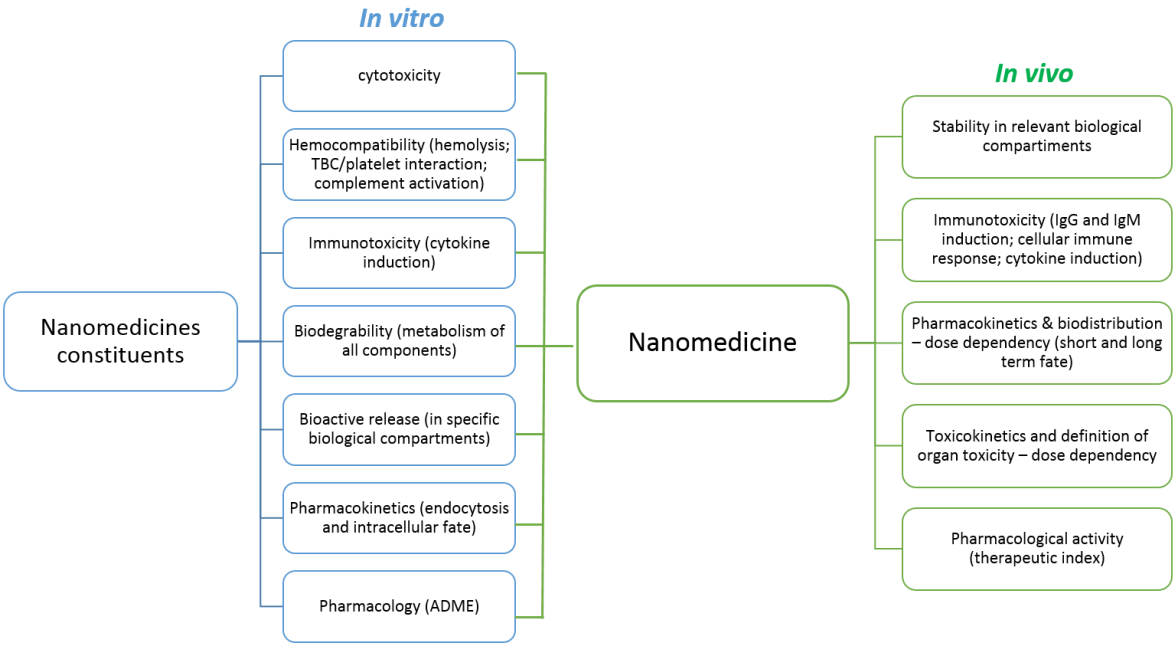

Figure 3 - Typical panel of tests used to define the preliminary safety of a nanomaterial (left) that is a candidate for incorporation into a nanomedicine, and the safety and efficacy of a nanomedicine (right). Adapted from *(1)*.

A first important issue in nanotoxicology is that the nanomaterials to be tested in a biological system (either *in vitro* or *in vivo*) are thoroughly characterized, so that meaningful, reproducible results are ensured. Nanoparticle analysis should involve purity certification, controlled morphology, polydispersity and solubility, conductivity or redox behaviour, among others, to provide reliable results on physical-chemical states and on stability. Typically, multiple measurement techniques must be adopted and applied to complex nanomaterial systems to accomplish validity since no single analysis can provide sufficient information to correlate nanoparticle characteristics with biological response *(27–29)*.

Biological testing of a nanomedicine or its components should then involve *in vitro* and/or *in vivo* testing. *In vitro* cellular tests are the most common assessment method used to understand the mechanisms of cell damage, including triggering of apoptosis and oxidative stress (cytotoxicity). These tests are easier to control and reproduce and less expensive than animal studies. Also, they provide a rapid and effective means to assess nanomedicines for a number of toxicology endpoints *(24,26,27)*. Controlling the experimental conditions such as temperature, pH, nutrient and waste concentration, as well as the nanomedicines concentration, assures that the measured cell death corresponds to the toxicity of the added nanomedicines and not to the unstable culture conditions *(30)*. Furthermore, *in vitro* assays

allow to use various cell lines, mimicking different tissue environments, and reactive pathological or inflammatory conditions likely observed *in vivo (12,28,31)*.

Several techniques can be used to assess the *in vitro* toxicity of nanomaterials, such as: assays for cell viability or proliferation; mechanistic assays (ROS generation, apoptosis, necrosis and DNA damaging potential); microscopic evaluation of intracellular localisation (comprising techniques like SEM-EDS, TEM, AFM, Fluorescence spectroscopy, MRI and VEDIC microscopy); gene expression analysis; *in vitro* hemolysis; and genotoxicity *(31)*.

Following combined results from *in vitro* cellular assays, nanotoxicity studies may be complemented with *in vivo* experiments to achieve validation and progress towards clinical development. *In vivo* experiments can potentially provide information on both the pharmacokinetics (i.e. the fate of the administered substance, including its absorption, distribution, metabolism and excretion), and pharmacodynamics (i.e. the effects caused on the organism). Hence, *in vivo* pharmacokinetics and pharmacodynamics studies are an essential part of nanomedicine evaluation and design *(23,28)*.

Regarding the mechanisms by which nanomaterials exert toxic effects, one of the main reported pathways is the generation of reactive oxygen species (ROS) and mitochondrial stress. ROS formation is also interconnected with cytoskeleton disorganization or damage, decreasing actin dynamics and reducing mitochondrial membrane potential via open voltage-dependent anion channels. This increases mitochondrial ROS release and cell apoptosis sensitivity *(12)*. The reduction of mitochondrial activity leads to a decrease in ATP production that is necessary for many cellular functions. Thus, screening for ROS in relation to the toxicity of nanomaterials is important since the production of ROS can result in inflammatory responses, apoptosis, necrosis, fibrosis, hypertrophy, metaplasia, and carcinogenesis *(12,33,34)*.

1.2.2. Toxicity of silk nanoparticles (SNPs)

Regarding the safety of SNPs, little information is available. Silk derived from natural sources or obtained through recombinant engineering approaches has been increasingly used for biomedical applications. However, although different silk formats (e.g. films, scaffolds, sutures) have demonstrated good biocompatibility, these data cannot be extrapolated to assure the safety of SNPs proposed for systemic administration. *In vitro* and *in vivo* studies are needed to support the safe transfer of SNPs across all stages of development *(10)*.

Some data of the SNPs internalization mechanisms suggest that endocytosis contributes to the uptake, trafficking rate and intracellular fate *(2)*. In a study by Kundu *et al.*, the nanoparticles internalization process was assessed by labelling the nanoparticles with FITC (fluorescence isothiocyanate) and observing the cellular uptake by confocal laser scanning microscopy (CLSM). The SNPs internalization occurred by endocytosis, and SNPs were mainly present in the perinuclear region, remaining viable and without causing any overt cytotoxicity *(24)*. Following, Seib's team examined SNPs intracellular fate by live confocal microscopy, confirming that SNPs enter the cells by endocytosis *(19)*.

The few studies which have investigated the cytotoxicity of SNPs through *in vitro* experiments suggested none or minimal toxicity. Human breast cell lines were shown to maintain their viability when exposed to SNPs of 35-120 nm diameter, at a concentration of 100 µg/ml for up to 24 hours, as assessed by the MTT assay *(24)*. Cell cycle analysis further revealed normal cell cycle distribution without any visible signs of cell cycle arrest *(19,24)*. Despite these results, further information on how SNPs interact with different cell types is needed for characterizing and understanding the SNPs safety profile *(19)*.

1.3.Metabolomics in nanomedicine/nanotoxicology

1.3.1. The metabolomics approach

The metabolome consists of the inventory of endogenous small molecules (with molecular mass lower than 1000 Da) present in a biological system as a result of intermediary cellular metabolism. Metabolomics (or metabonomics) is concerned with the comprehensive identification and quantification of metabolites in biological systems (cells, tissues, body fluids) and of their changes in response to pathophysiological stimuli or genetic modification *(35,36)*.

Since metabolites play a very important role in connecting the different pathways that operate within a living cell, metabolomic studies are an important part of integrated system's biology approaches, used to study pathological processes or the effects induced by different external stimuli (e.g. drugs, nanomaterials) *(37)*. Assessing the metabolic profiles or signatures potentially allows to estimate cellular function and the overall physiological status of an organism *(38)*. Indeed, many pathological conditions can be reflected by changes in metabolite levels, as shown by the increasing number of metabolomic studies in the field of disease diagnosis and monitoring. The most widely investigated classes of diseases include cancer, diabetes, cardiovascular and neurological diseases. Metabolomics technologies also have the potential to provide rapid screening for biomarkers of toxicity, showing great promise in drug toxicological assessment and development, as well as in the fields of nanotoxicology and nanomedicine *(38)*.

Several sample types with different complexity can be retrieved for metabolomics studies, from cell cultures to tissues and biofluids of animal models or human subjects *(34,38)*. Nuclear Magnetic Resonance (NMR) spectroscopy and mass spectrometry (MS) (the latter being typically coupled to different chromatographic techniques, such as liquid or gas chromatography) are the most often employed methods for metabolome profiling. These techniques are the major tools to detect global changes in the metabolome because they allow a large number of metabolites to be detected simultaneously and non-selectively *(34,39)*. Compared to MS, NMR is less sensitive, with detection limits in the sub-milimolar range, but it offers advantages in terms of high reproducibility and non-destructiveness (allowing sample recovery for further analysis). Moreover, it allows the direct analysis of cells, tissues and biofluids, with minimal sample interference, and it is quantitative in nature, providing a large amount of structural and quantitative information in a single record *(34,38)*. As NMR

has been the technique used in this work, its basic principles will be briefly described in the following section.

1.3.2. Basic principles of Nuclear Magnetic Resonance (NMR) Spectroscopy

The nuclei of certain atoms possess an overall spin (I) different from zero, which makes them detectable by NMR. These nuclei include, for instance, the isotopes ^{1}H, ^{13}C, ^{31}P, ^{15}N (I = ½) and ^{2}H, ^{14}N (I = 1). The hydrogen isotope (^{1}H) is the most commonly observed nucleus in NMR metabolomics due to its ubiquity in metabolites and high natural abundance (99.98 %) *(40)*.

The nuclear spin generates a magnetic dipole moment μ, which in the presence of an external magnetic field B_0 aligns in a discrete number of orientations, corresponding to different energy levels. NMR spectroscopy is based on the transition between these energy levels *(40,41)*. For nuclei with spin I = ½, like protons, there are two possible orientations, parallel and anti-parallel to B_0, each characterized by a magnetic quantum number m and a different energy level (Figure 4). At the equilibrium state, there is an excess of nuclei at the lower energy level, but when an oscillating magnetic field B_1 is applied, through a radiofrequency (RF) pulse, transition to the higher energy level occurs and the nuclei become excited. Once the RF pulse is turned off, the nuclei return back to equilibrium, through relaxation, and this process is recorded as a time domain signal called the free induction decay (FID). The FID is then transformed into a frequency domain spectrum through Fourier transform (FT) *(41)*.

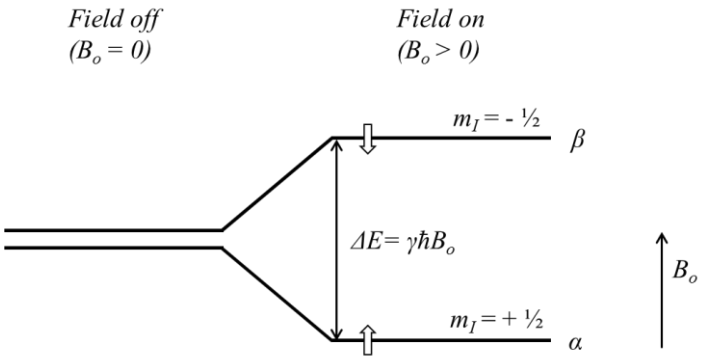

Figure 4 - Schematic representation of the nuclear spin energy levels of a spin- ½ nucleus in a magnetic field. The energy difference between the two states is given by $\Delta E = \gamma\hbar B_0$, where ΔE is the energy difference between the two states, m_I the magnetic quantum number, $\hbar = h/2\pi$ (where h is Planck's constant) and B_0 the magnetic field. Adapted from *(41)*.

The different signals in the NMR spectrum of a molecule arise from the different electronic environments of the nuclei, because the bonding electrons create their own small magnetic field; thus, each proton (or group of equivalent protons) resonates at a specific frequency, giving rise to signals in different positions of the NMR scale. This scale is calibrated to the frequency of a reference compound (e.g. tetramethylsilane, TMS) and the frequency values are converted to parts per million (ppm). The resulting chemical shift scale (in ppm) is independent of B_0, thus allowing chemical shifts obtained from different instruments to be compared *(42)*. The ^1H absorption regions of some characteristic functional groups are comprised within the narrow range of 0 – 14 ppm: saturated hydrocarbons generally absorb between 1.0 and 4.0 ppm, whereas the olefinic protons appear in the region of 5.0 – 6.5 ppm and the resonances of aromatic protons are in the region of 6.5 – 8.5 ppm *(41)*. Figure 5 shows the typical ^1H chemical shift ranges of some functional groups in organic compounds.

Another characteristic feature of NMR signals is that they are often split into several lines due to nuclear spin-spin interactions mediated through the electrons of the chemical bonds, and known as scalar coupling. The multiplicity and magnitude of the splittings (coupling constants, *J*) provide knowledge about the number of neighbouring protons and their bond connectivities *(40)*.

Finally, it is also important to mention that signal area is proportional to the number of protons that originate the peak, hence, to compound concentration. Therefore NMR is inherently quantitative and it can be used for quantification purposes *(40,43)*.

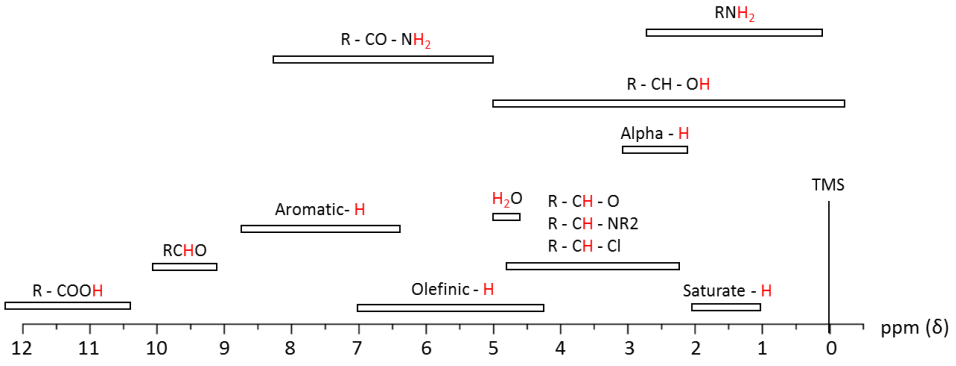

Figure 5 - Typical ^1H chemical shift ranges (in ppm) of some functional groups. Based on *(41)*.

1.3.2.1. Main one- and two-dimensional NMR experiments in metabolomics

The biological samples usually analysed in metabolomic studies (biofluids, tissues and cells) typically show complex profiles, comprising many overlapped signals, and a strong water signal which needs to be suppressed as it would otherwise dominate a large section of the spectrum and cause dynamic range problems *(37)*. This is typically achieved by the 1D NOESY (nuclear Overhauser effect spectroscopy) pulse train with presaturation during relaxation delay and mixing time (standard water presaturation used in this work), the WET sequence (water suppression enhanced through T_1 [spin lattice relaxation] effect) or the Watergate water suppression scheme *(44)*.

To deal with spectral overlap and identify the metabolites present in complex biological samples, 2D NMR experiments are usually employed, as they allow increasing the signal dispersion and revealing molecular connectivities. The more commonly used 2D experiments include: correlation spectroscopy (COSY) and total correlation spectroscopy (TOCSY) experiments that provide spin-spin coupling connectivities (usually over 3-5 bonds), giving information on which signals belong to the same spin system; J-resolved spectroscopy (JRES), that allows spectral simplification, minimizing overlap due to contributions of substances with short ^{1}H spin-spin relaxation times (T_2) and helping to determine coupling constants; and inverse-detected heteronuclear correlation methods such as heteronuclear single quantum correlation (HSQC), where signals correspond to ^{1}H's and ^{13}C's directly bound. *(41,45)*.

1.3.3. Multivariate analysis: principles and tools

After data acquisition and processing, metabolite signals are usually subjected to multivariate statistical analysis to detect consistent variation patterns (figure 6) *(34)*. Indeed, since each spectrum comprises a wide range of variables (metabolites) and numerous spectra are often acquired within a study, multivariate analysis (MVA) is required to reduce data complexity and extract meaningful biochemical information. MVA usually involves the application of unsupervised methods such as Principal Component Analysis (PCA) and hierarchical cluster analysis (HCA), together with supervised methods such as Partial Least Squares – Discriminant Analysis (PLS-DA), where information about sample class is provided and class separation is maximized *(34)*.

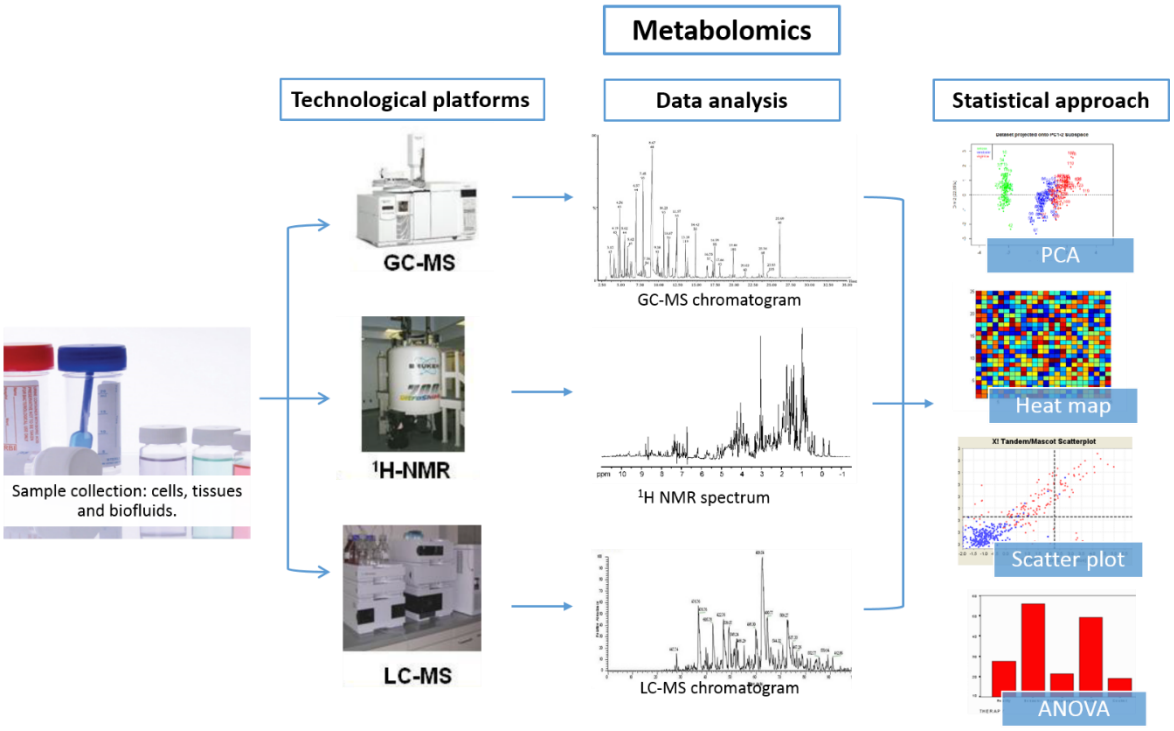

Figure 6 – General overview of the typical strategy followed in metabolomics studies. Adapted from *(95)*.

Principal Component Analysis (PCA) and Hierarchical Cluster Analysis (HCA) are very useful for revealing grouping trends and outliers in a sample set. The idea behind PCA is to explain the original data variance in a lower dimensional space defined by Principal Components (PC's), which are linear, uncorrelated combinations of the original variables *(46)*. Through PCA, the original data matrix X is decomposed into a scores matrix (T), a loadings matrix (P) and a residuals matrix E (part of X that is not explained by the model), according to the following equation: $X = TP^t + E = t_1p_1^t + t_2p_2^t + E$ (where t denotes the transpose). The first PCA component ($t_1p_1^t$) contains the largest matrix variance, the second component the second largest variance, and so on, so that all components are mutually orthogonal to each other *(47,48)*.

By projecting the observations (spectra) into the new PC-coordinate system, we obtain a scores plot (Figure 7), which allows visualizing the trend for samples to group together or to separate along one axis, according to their similarities or differences. Moreover, by plotting the corresponding loadings, we obtain information about the original variables that are responsible for the sample distribution observed in the scores plot.

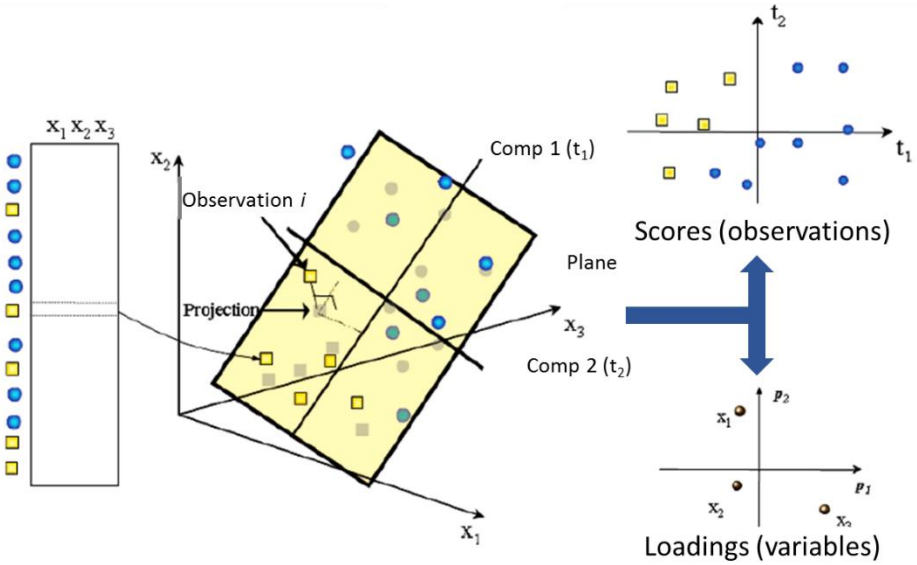

Figure 7 – Schematic representation of a principal component analysis model. Adapted from *(47)*.

Hierarchical Cluster Analysis is an exploratory multivariate analysis method that allows the cluster structure of a dataset to be detected and the hierarchical relationship of the clusters to be revealed. This unsupervised approach enables samples to be grouped according to their dissimilarity or similarity, usually called distance, in the variable space. To unveil the clusters and trends, the distance matrix is calculated and an agglomerative clustering algorithm is performed. Based on that algorithm, a final dendrogram is constructed representing in which the closest clusters are most similar. Thus, this technique improves the understanding of the structure of the dataset, presenting visual information of the cluster structure *(46,49,50)*.

Unlike PCA and HCA, supervised methods like PLS-DA allow maximizing the separation between pre-defined classes (e.g. control/exposed, low/high dose, etc.), facilitating the interpretation of the differences between them *(46,47)*.

While PCA and HCA are methods that only consider the structure of the data matrix, *X*, PLS models the relationships between the data matrix *X* and a second matrix, *Y*, which can either contain quantitative (e.g. concentration of endogenous metabolites) or qualitative

values (e.g. class membership). In the latter case, it is typically used in conjunction with discriminant analysis (PLS-DA), which is very useful in metabolomics studies aiming at differentiating sample classes.

In PLS, the new variables (called latent variables, LVs) are calculated not only to model the variance in X (as in PCA) but also its correlation with Y, according to the following equations:

$X = TP^t + E$

$Y = TC^t + F$

Where *T* is the matrix of the extracted scores (of both *X* and *Y*), *P* and *C* are the loadings matrices, and *E* and *F* the residuals of *X* and *Y*, respectively *(37,51)*. The T scores are linear combinations of the original X variables and the weights (W) which define the quantitative relationship between X and Y.

Similarly to PCA, the results of PLS-DA can be visualized through scores and loadings plots. Additionally, the loadings may be coloured as a function of variable importance in the projection (VIP) to highlight the most discriminant metabolites (those with VIP > 1).

1.3.4. Univariate statistics

In order to assess the statistical significance and magnitude of variations in individual metabolites, univariate statistics may be applied, complementary to MVA. Commonly used methods include the *t*-test, the Wilcoxon test (if data are not normally distributed), effect-size estimation, and analysis of variance (ANOVA) *(46,52)*.

In the context of this thesis, the Shapiro-Wilk test was primarily performed in order to test for normality. For normally distributed data, the *t*-test was performed, while for nonparametric metabolites, the Wilcoxon test was used. These methods allowed to statistically evaluate the significance of the difference in average metabolite levels *(53,54)*.

The *t*-test is a standard statistical approach to examine if a study's result is statistically significant through the null hypothesis (no difference between the means compared). For that purpose, the probability for the null hypothesis rejection (*p*-value) is determined at a pre-established significance level; typically, a difference between group means is considered statistically significant if the *p*-value is inferior to 0.05. However, the *p-value* does not provide crucial information about the magnitude of the variation of interest or its precision, besides being influenced by sample size *(55)*. To deal with these limitations, another

statistical parameter, the effect size (*d*), has been increasingly used *(56)*. This parameter, calculated according to the equations below (1 and 2), gives an indication of the magnitude of the variation, while accounting for the standard deviations (s_1 and s_2) associated with the means compared ($\bar{x}_1$ and $\bar{x}_2$) and the number of samples (n_1 and n_2). Moreover, it is less sensitive to sample size, allowing increased confidence when comparing small sample sets. For the standardized mean differences between two groups, Cohen *et al*. *(57)* classified effect sizes as small ($d = 0.2$), medium ($d = 0.5$), and large ($d \geq 0.8$). The 95 % confidence interval (CI) around the standardize mean differences is calculated according to equation 3 *(55,56)*.

$$d = \frac{\bar{x}_1 - \bar{x}_2}{s} \qquad \textbf{Equation 1}$$

$$s^2 = \frac{(n_1 - 1) \times s_1^2 + (n_2 - 1) \times s_2^2}{(n_1 + n_2) - 2} \qquad \textbf{Equation 2}$$

$$d \pm 1.96 \sqrt{\frac{n_1 + n_2}{n_1 n_2} + \frac{d^2}{2(n_1 + n_2)}} \qquad \textbf{Equation 3}$$

1.3.5. Metabolomics applications in nanomedicine/nanotoxicology: state-of-the-art

While metabolomics has been extensively applied in the fields of disease diagnosis or toxicology, the applications in nanomedicine/nanotoxicology are still scarce. In the next subsections, metabolomic studies of the impact of different NPs on either cellular or animal models will be reviewed. A list of those studies is summarised in Table II. To our knowledge, no studies on silk nanoparticles have been reported, this thesis constituting the first account on the subject.

1.3.5.1. Silica (SiO_2NPs) nanoparticles

Silica nanoparticles (SiO_2NPs) are increasingly used in the biomedical field, mainly due to their excellent solubility and high stability, and can enter biological systems through numerous routes. Despite their favourable biocompatibility, some investigations have revealed that silica NPs exposure exerts adverse effects such as cytotoxicity and oxidative

stress *(58–60)*. In addition, there have been reports of inflammatory responses, hepatotoxicity, and fibrosis following exposure *(34)*. As shown in table II, a few studies have addressed the cellular and *in vivo* responses to SiO_2NPs by metabolomics, using different analytical techniques (^{1}H NMR spectroscopy, GC/MS and LC/MS). The cytotoxicity of the NPs was demonstrated by a significant metabolic shift between control and treated cells. In one of such studies, cell metabolic variations revealed to be dose-dependent, causing compositional changes related to membrane degradation, catabolism of carbohydrates and proteins, and oxidative stress response *(60)*. In particular, the authors reported increases in some lipids, like triglyceride, LDL, VLDL, and in lactate/alanine ratio, together with decreases in several amino acids, ATP and other metabolites *(60)*. In another study, after the treatment with SiO_2NPs, cellular amino acids were down regulated and, on the contrary, urea was up regulated. Moroever, higher levels of lysophosphatidylcholine (LPC) and lysophosphatidylethanolamine (LPE), and decreased levels of reduced glutathione (GSH) were reported, based on LC/MS measurements. LPC and LPE have been postulated to be biomarkers of biochemical injury arising from cellular toxicity *(59)*. Another study with Kupffer cells (KC) indicated that SiO_2NPs cause hyperplasia, hepatic inflammation, and oxidative stress, which lead to changes in the biochemical composition of the liver. After the exposure to SiO_2NPs, KC released bioactive mediators, such as ROS, TNF-α, and NO, which subsequently contributes to hepatotoxicity *(58)*. The significantly altered metabolites are involved in energy, amino acid, lipid and nucleotide metabolism, indicating impairment of the Krebs cycle and the occurrence of oxidative stress *(34,58–60)*.

The toxicological effects induced by SiO_2NPs can drastically change based on particle formulation, size, shape and type. Metabolomic variations and compositional changes due to toxicological effects can provide much better understanding of SiO_2NPs and their metabolic fate, offering a chance to better define the bio-safety of this biomaterial *(60–62)*.

1.3.5.2. Iron oxide nanoparticles

Ultra-small superparamagnetic particles of iron oxide (USPIO) are excellent tools in the biomedical field since they can be functionalized for various applications and guided by an external magnetic source. These compounds have been developed as intravenous contrast agents for early detection of abnormal tumour associated lymph node and bone marrow, as well as contrast agent to improve magnetic resonance imaging (MRI) *in vivo*. In general, they are classified as biocompatible, showing no severe toxic effects *in vitro* or *in vivo*.

However, the potential biotoxicity and the disturbances of hepatic, renal and cardiac functions were derived from metabolomics data following USPIO administration *(30,63,64)*.

Feng and his colleagues have demonstrated varying effects of USPIO on the metabolic profile of different tissues including kidney, liver and spleen of rats, through High Resolution Magic Angle Spinning (HRMAS) ^{1}H NMR. An intravenous injection (tail vein) of coated-USPIO was administrated to rats, and the harvested tissue samples reflected several effects in metabolic pathways including energy, lipid, glucose, and amino acids metabolism. The disturbance and impairment of biological function in these specific organs were dependent on the particles size and surface chemistry of USPIO *(64)*. In another Feng's study, metabolomic analysis revealed USPIO-induced metabolic changes in the blood of injected animals. Plasma samples showed a relative increase in intermediates of the Krebs cycle such as succinate and citrate, in glucose, and in the end-products of glycolysis such as lactate and acetate. USPIO administration also led to elevation of plasma inositol, choline and glycerophosphocholine. Similar changes in triglycerides and cholesterol were observed from clinical biochemistry and metabolomic analysis of NMR data derived from rat plasma. The metabolic changes in VLDL and HDL were suggested to be possibly related to USPIO-induced renal failure and a risk factor for coronary heart disease *(65)*.

1.3.5.3. Gold and silver nanoparticles

Gold and silver nanoparticles have received special attention since they have a great potential for applications in drug delivery systems, ultrasensitive chemical and biological sensors, as catalysts and in therapy *(66)*.

Generally, gold nanoparticles provide non-toxic routes to drug and gene delivery application, being able to deliver large biomolecules (peptides, proteins, or nucleic acids). Moreover, gold nanorods (Au NR) can be applied to amplify the biorecognition of anticancer drugs, emerging as one of the most promising putative anti-tumour treatments. Extensive research have been performed on the cytotoxicity, biocompatibility and biodistribution of several Au NR with different physicochemical properties like size, shape and surface group modifications *(66,67)*. Zhang and his team have studied metabolic changes in tumour and normal cells after exposure to protein-coated Au NR, through ^{1}H NMR. Their results showed time-dependent and cell-specific metabolic response of tumour cells and normal cells. Protein-coated Au NRs exposure modulated the micro-environment of cells by suppressing the levels of lactate, which might be vital for cancer growth, but also induced severe

oxidative stress and subsequent cell death in tumour cells whilst the normal ones survived. Normal cells had an overwhelming antioxidant capability as a result of activated glutathione synthesis and transformation into GSSG during the process of scavenging free radicals. This experiment provided important information in designing anti-cancer drugs to destroy only cancer cells and not normal and healthy cells. Moreover, metabolomics helped to elucidate molecular mechanisms of anti-cancer drugs action *(67)*.

Silver is used in consumer products as nanoparticles (Ag NPs) in refrigerators, toothpastes and health drinks. For that reason, it is important to understand the potential physiological, pharmacological and toxicological properties of silver. Ag NPs have displayed only minimal toxicity in animal studies and good biocompatibility, however, little information is available on the mechanism of action of silver nanoparticles in mammals *(66,68)*. Hadrup's team employed metabolomic investigation with HPLC separation and quadrupole time-of-flight (QTOF) accurate mass detection to investigate the whole metabolome in the urine of rats. After silver administration, uric acid and allantoin were found to be increased in female rat urine. One possible explanation for this increased purine metabolism could be the induction of oxidative stress and cytotoxicity with simultaneously DNA degradation. This was supported by *in vitro* studies, where ROS were found increased *(68)*.

In another study, Li's team have found that *Daphnia magna* exhibited significant changes in their metabolic profile following the two size Ag NP and Ag^+ exposure. Most of the metabolic biomarkers for Ag NP exposure were identical to those of the Ag^+-exposed groups, suggesting that the dominant effects of both Ag NPs were due to release of Ag^+. The observed metabolic response to the Ag^+ released from both the Ag NPs is an indicative of disturbances of energy metabolism and oxidative stress in *D. magna*. Moreover, the levels of lactate were elevated in all Ag NP-treated groups but not in the Ag^+-treated groups. This suggests a mechanism of enhancement of anaerobic metabolism being induced by Ag NPs *(69)*.

1.3.5.4. Titanium dioxide (TiO_2) nanoparticles

Due to their high stability, anticorrosion and photocatalytic properties, TiO_2NPs are abundantly produced and capable of a great variety of applications in life science and industry, such as paints, coatings, plastics, skin care products, foods and some pharmaceuticals. However, some studies reported that TiO_2NPs can cause pulmonary

inflammation, fibrosis and DNA damage, while chronic exposure can be carcinogenic. *(70,71)*. Still, the biological effects of TiO_2NPs exposure and the mechanism underlying the body response are still not well established. In order to elucidate the pathological, metabolic and toxicological response, metabolomic techniques were employed *(70–73)*.

In one of those studies, metabolomic response to TiO_2NPs treatment supported *in vitro* findings that reported cellular toxicity and induction of oxidative stress upon treatment of HaCaT cells with TiO_2NPs. Samples were analysed by either gas chromatography/mass spectrometry (GC/MS) or liquid chromatography/mass spectrometry (LC/MS) where several metabolites were found significantly altered, such as coenzyme A, carnitine and acyl-carnitines. Also, a lower level of nucleosides and nucleotides was observed. These changes indicated that TiO_2NPs have significant effects on anabolic pathways and energy metabolism *(71)*. In another study, numerous changes in endogenous metabolites were observed in the ^{1}H NMR spectra of female Wistar rats' urine and serum samples following TiO_2NPs administration. TiO_2NPs were suggested to cause disturbances in energy metabolism, amino acid metabolism and gut microflora, which may be attributable to their toxic effects on the liver and heart *(70)*. Earthworms have also been exposed to TiO_2NPs and the metabolomic response revealed increased levels of alanine and other amino acids and decreased maltose, reflecting significant alterations in the underlying network of earthworm metabolic pathways *(72)*.

With Garcia-Contreras' team research, it was found that TiO_2 NPs significantly reduced most of amino acids, while, ophthalmate, a-aminoadipate, kynurenine and β-alanine increased. Notably, many metabolites in urea cycle, including asparagine, arginine, argininosuccinate, citrulline, ornithine and the metabolites in its downstream polyamine pathways, such as putrescine and spermidine also decreased, indicating that the activation of urea cycle and polyamine pathway was stronger than those of the other pathways. TCA cycle metabolites also showed different patterns. First, citrate, cis-aconitate and isocitrate showed a gradual decrease, possibly using the acetyl-CoA produced by oxidative decarboxylation of pyruvate. Second, a-ketoglutarate, succinate, fumarate and malate remained almost constant. Metabolic changes were also seen in the levels of GSH and GSSG, where the concentration of GSH was nearly one order higher than that of GSSG, which favoured the cells toward oxidative state *(73)*.

1.3.5.5. Micellar nanocarriers and liposomes

Micellar nanocarriers are self-assembling nano-sized colloidal particles with a hydrophobic core and hydrophilic shell. Nowadays they are successfully used as pharmaceutical carriers for low water solubility drugs and have demonstrated a series of attractive properties as drug carriers since they can overcome some toxicities caused by the toxic organic excipients of the drugs *(74,75)*. Katragadda's team has performed ^{1}H NMR of mice tumour extracts in different treatment groups noticing significantly altered metabolic activities. The results suggested that paclitaxel/17-AAG loaded micelles normalized glucose consumption in the tumour by reducing glucose uptake and blocking aerobic glycolysis. This led to significantly decreased levels of glucose in the tumour, as well as lactate and alanine, which are end products of glycolysis *(75)*.

Liposomes are small vesicles composed of one or more lipid membranes surrounding discrete aqueous compartments. These vesicles can encapsulate water-soluble drugs in their aqueous spaces and lipid-soluble drugs within the membrane itself. A liposomal drug delivery system can alter the *in vivo* behaviour, attenuate adverse side effects and improve the therapeutic index of the encapsulated drug. Cong's team performed a urine metabolic study based on UPLC/TOF-MS for the assessment of cumulative cardiotoxicity in rats. Their study showed that the drug pirarubicin (THP) causes systemic or cardiac toxicity via a significant decrease in the intermediary metabolic pathways associated with the key energy production. Thus, a diminution of metabolites associated with the TCA cycle, glycolysis, pentose phosphate and amino acid synthesis pathways was observed. These considerations are important for the safety assessment of liposomal drug delivery system *(76)*.

Table II – Overview of metabolomic studies of nanomaterials with biomedical applications.

Nanomaterial	*Cell model*	*Animal model*	*Analytical technique*	*Sample type*	*Year of publication (Ref.)*
SiO_2 NP	HeLa	-	^{1}H NMR (HRMAS)	Cell extracts	2013 *(60)*
	MRC-5	-	GC/MS or LC/MS	Cell extracts	2012 *(59)*
	-	Sprague Dawley rats	^{1}H NMR	Liver tissue	2013 *(58)*
USPIO	RAW264.7	-	^{1}H NMR (HRMAS)	Cell extracts	2011 *(63)*
	-	Sprague Dawley rats	^{1}H NMR (HRMAS)	Tissue	2011 *(64)*
	-	Sprague Dawley rats	^{1}H NMR	Urine and plasma	2010 *(65)*
Au NP	A549; 16-HBE	-	^{1}H NMR	Cell extracts	2013 *(67)*
Ag NP	-	Wistar Hannover Galas rats	HPLC-QTOF-MS	Urine	2012 *(68)*
	-	*Daphnia magna*	^{1}H NMR	Metabolite extracts	2015 *(69)*
TiO_2 NP	HaCat	-	GC/MS or LC/MS	Cell extracts	2013 *(71)*
	-	*Eisenia fetida* earthworms	^{1}H NMR	*E. fetida* tissue	2011 *(72)*
	-	Wistar rats	^{1}H NMR	Urine and serum	2010 *(70)*
	HGF	-	CE-TOF-MS	Cell extracts	2015 *(73)*
Micellar nanocarriers	-	Human ovarian cancer SKOV-3 cells xenograft in mice	^{1}H NMR	Tumour tissue	2013 *(75)*
Liposomes		Sprague Dawley rats	UPLC/TOF–MS	Urine	2012 *(76)*
Cu NP	-	Wistar rats	^{1}H NMR	Urine and serum	2008 *(77)*
ZnO_2 NP	-	Rats	^{1}H NMR	Urine and kidney aqueous extracts	2012 *(78)*

Note 1 – Abbreviations: Silver (Ag); Gold (Au); Copper (Cu); Silica dioxide (SiO_2); Titanium dioxide (TiO_2); Ultrasmall Superparamagnetic Iron Oxide (USPIO); Zinc dioxide (ZnO_2); Henrietta Lacks' cells (HeLa); Human Fetal Lung Fibroblast Cells (MRC-5); Mouse leukemic monocyte macrophage cell line), (RAW264.7); Adenocarcinomic human alveolar basal epithelial cells (A549); Human bronchial epithelial cells (16-HBE); spontaneously immortalized, Human keratinocyte line (HaCat); Human gingival fibroblast cells (HGF); High-performance liquid chromatography (HPLC); Quadrupole-time-of-flight (QTOF); Mass spectrometry (MS); Nuclear Magnetic Resonance (NMR) Spectroscopy; Ultra Performance Liquid Chromatography (UPLC); Gas Chromatography (GC); Liquid Chromatography (LC); High Resolution Magic Angle Spinning (HRMAS).

1.4. Scope and aims of this thesis

The main goals of this work were:

i) To characterize the metabolic profile of the macrophage cell line RAW 264.7.

Macrophages are specialized host defence cells found in the reticuloendothelial system, responsible for maintain cellular and organism homeostasis *(12,79,80)*. Through an endocytic process, macrophages play an important role in the uptake of NPs from the circulation, their metabolism and degradation, thus being considered a relevant model for nanotoxicological studies. Thus, they were selected for this study and it is expected that their metabolic content may be reflective of their biochemical status.

ii) To assess the impact of silk nanoparticles (SNPs) on macrophage metabolism, by identifying the most affected metabolites and pathways.

Both aqueous and lipid cell extracts were considered for this purpose in order to obtain a more comprehensive view of the metabolome.

iii) To examine the dependence of metabolic effects on exposure concentration and duration.

Three time points and two SNPs concentrations, selected, respectively, based on the cells growth curve and viability assays, were tested.

iv) To evaluate the sensitivity of NMR metabolomics to provide mechanistic insight into cell-NPs interactions.

CHAPTER 2 – Experimental Section

2.1. Materials and methods

This work has been carried out in the framework of a collaboration with the Strathclyde Institute of Pharmacy and Biomedical Sciences of the University of Strathclyde, Glasgow (UK), where cell culture studies and samples for the metabolomics studies were prepared and collected by Dr P. Seib. The NMR acquisition, processing and analysis were then performed at the University of Aveiro, within the framework of this thesis.

2.1.1. Silk nanoparticles (SNPs)

Uncoated, spherical silk nanoparticles (ca. 100 nm in diameter) were generated at Strathclyde from *B. mori* silk, according to the procedure described in *(19)*. For all cell exposure experiments, a 10 mg/ml stock in ddH_2O was generated and gamma sterilised.

2.1.2. Cell culture studies

Murine RAW 264.7 macrophages were seeded at a density of 1.5×10^4 cells/cm^2, the required cell density to provide a sufficiently strong signal for NMR analysis. For proliferation and cytotoxicity studies, cells were seeded in 100 μL of complete medium into 96 well plates. For metabolomics studies, 60 mm diameter Petri dishes were used and scaled accordingly. For all studies, cells were plated and then allowed to recover over night before commencing measurements.

In order to establish the cells growth curve, cell proliferation was monitored using MTT (5mg/mL in PBS). Briefly, cells were incubated with 20 μL of MTT for 5 h. Next, the medium was aspirated and replaced with 110 μL of DMSO and incubated for 10 minutes to dissolve formazan crystals. Finally, 100 μL of the product was transferred to a reading plate and absorbance was measured at 570 nm. Data were expressed as a percentage of the maximum absorbance determined in this study.

2.1.3. Cytotoxicity assessment of SNPs

The cytotoxicity of SNPs was assessed using the colorimetric MTT assay, which measures the formation of purple formazan. Cell viability was calculated as a percentage by using untreated cells as a benchmark for 100% viability, since the tetrazolium salt MTT can only be metabolized by living cells. Therefore, the dye intensity is proportional to the number of viable cells *(81)*. Briefly, cells were incubated with a 2.5 to 1000 μg/mL SNPs;

5h before the end of a 24h, 48h and 72h exposure time 20 μL of MTT was added to cells and incubated. Next, the medium was aspirated and replaced with 100 μL of DMSO and absorbance was measured at 570 nm.

2.1.4. Samples for metabolomics studies

For metabolomics, macrophages were exposed to two concentrations of SNPs (low, 10 μg/mL and high, 500 μg/mL) and three sample types collected from each dish: culture medium, cell aqueous extract and cell lipid extract. Samples from control dishes (no SNPs added) were also collected. Four independent assays were performed (with duplicates for controls), so that for each concentration of SNPs, there were four dishes, whereas eight dishes were available for controls.

After collecting and centrifuging a medium aliquot, the remaining medium was aspirated and each dish was washed twice with PBS. Then, intracellular aqueous metabolites and lipids were extracted using a dual phase extraction procedure adapted from Teng *et al. (82)*. Briefly, 650 μL of cold methanol 80% was added, to stop metabolic activity, and the cells were scraped off the dish and vortexed for 1 min in microcentrifuge tubes containing 0.5 mm glass beads, to aid cell breakage. Chloroform (260 μL + 260 μL) and water (220 μL) were then added to each sample, each addition being followed by 1 min vortexing, and the samples were left to rest on ice for 10 min. After centrifuging at 2000g for 15 min, the upper aqueous phase and the lower organic phase were then carefully transferred into new vials, dried under vacuum and stored at -80ºC. The dried samples were sent by express mail and stored at -80ºC until NMR analysis.

2.2.NMR Spectroscopy

2.2.1. Sample preparation for NMR

Dried aqueous samples were reconstituted in 600 μL of deuterated phosphate buffer (PBS, 100mM, pH 7.4) containing 0.1 mM TSP, while organic phase extracts were reconstituted in deuterated chloroform containing 0.03% TMS. For NMR analysis, 550 μL of each sample were transferred into 5 mm NMR tubes. The medium samples remain stored for later analysis and will not be considered within this thesis.

2.2.2. Acquisition and processing of ^{1}H NMR spectra

All experiments were acquired on a Bruker Avance DRX spectrometer operating at 500.13 MHz for ^{1}H, using a 5 mm TXI probe, at 298 K. Standard 1D spectra (pulse programs 'noesypr1d' and 'zg' in Bruker library, for aqueous and lipid extracts respectively) were acquired with a 6510 Hz spectral width, 32 K data points, a 2 s relaxation delay (d1), and 256 scans. Data processing was performed using TopSpin 3.2 (Bruker Biospin, Rheinstetten, Germany). The free induction decay (FID) signals were processed by exponential multiplication (using a line broadening window function LB 0.3 Hz) and zero filling to 64 K data points prior to Fourier transformation. All 1D spectra were manually phased and baseline corrected. The chemical shifts were referenced internally to the TSP/TMS signal at δ 0.00 ppm (aqueous/lipid extracts). 2D ^{1}H-^{1}H total correlation (TOCSY) spectra, ^{1}H-^{13}C heteronuclear single quantum correlation (HSQC) spectra and *J*-resolved spectra were also registered for selected samples to assist spectral assignment. The main acquisition and processing parameters for these experiments are provided in the following tables:

Table III – Main parameters used for the acquisition and processing of 1D ^{1}H NMR (500 MHz) spectra of aqueous and lipidic extracts.

1D ^{1}H NMR (500 MHz)	
Acquisition parameters	
Experiment	standard 1D
Pulse programme [a] (aqueous/lipid extracts)	*noesypr1d/zg*
Number of scans, NS	256/256
FID data points, TD	32768/32768
Spectral width (ppm)	14.00/14.00
Acquisition time, ACQ (s)	2.34/2.34
Relaxation delay, RD (s)	2/2
Mixing time, tm (ms) (aqueous extracts)	100
Processing parameters	
Window function	exponential
Spectrum data points, SI	65536
Line broadening, LB (Hz)	0.3

[a] Bruker library

Table IV - Main parameters used for the acquisition and processing of 2D NMR (500 MHz) spectra of aqueous and lipid extracts.

2D NMR (500 MHz)			
	Acquisition parameters		
Experiment	^{1}H-^{1}H TOCSY	^{1}H-^{13}C HSQC	*J* – Resolved
Pulse programme [a]	*dipsi2phpr*	*hsqcetgp*	*jresgpprqf*
FID data points 1st dimension [F1]	4096	4096	8192
FID data points 2nd dimension [F2]	156	200	40
Number of scans	96	128	80
Spectral width [F1] (ppm)	16.02	16.02	16.02
Spectral width [F2] (ppm)	16.02	165.6	0.09
Relaxation delay, RD (s)	2	4	2
Mixing time, tm (ms)		30	
	Processing parameters		
Spectrum data points [F1], SI	4096	4096	16384
Spectrum data points [F2], SI	2048	2048	1024
Line broadening [F1], LB (Hz)	0.3/0.3	0.3	0.3
Line broadening [F2], LB (Hz)		1.0	0.3

[a] Bruker library;

2.3.Multivariate analysis

2.3.1. Pre-treatment and multivariate analysis of NMR spectra

The preparation of NMR data for multivariate analysis (MVA) requires the construction of data matrices ($n \times m$ (rows × columns) of *n* observations (samples) and *m* variables (peak intensities)), either using the full spectra or spectral regions (buckets). In this work, 0.01 ppm buckets were considered, after excluding selected regions for building the data matrix, namely the suppressed water signal (in aqueous extracts only) and additional signals found to result from contamination, either from the medium not completely washed off the dishes or from solvents present in the evaporation system (see table V). Each spectrum was exported from Amix-Viewer (version 3.9.14, BrukerBiospin, Rheinstetten) and normalized by total spectral area, in order to make the data from all samples comparable with each other.

Using SIMCA – P 11.5 software (Umetrics, Umeå, Sweden), the resulting data were scaled to Unit Variance (UV), giving equal variance to all variables, and PCA and PLS-DA were applied. The results were obtained in the form of scores scatter plots, representing the distribution of samples in the model, and corresponding loading plots, to provide information on which metabolites were responsible for the pattern observed in the scores plot. The loading profiles were obtained by multiplying the loading weights *w* (representative of the correlation of the *x* variable of the NMR spectra with *y* class), by the standard deviation. Next, the loadings were coloured by the variable importance in the projection (VIP), for the discrimination between the classes, using the R software version 2.15.0 (R Development Core Team, Vienna, Austria, 2012). To evaluate the quality of the models, a default seven-fold internal cross validation was used, from which R^2 and Q^2 values, respectively reflecting explained variance and predictive capability, were extracted. Generally, the values of Q^2 between 0 and 1 suggest some predictive character but the reliability increases as Q^2 approaches 1. However, higher R^2 and Q^2 values are desirable *(83)*.

Hierarchical cluster analysis (HCA) was also performed, based on the Pearson correlation coefficient with single linkage, using the GENE-E software (http://www.broadinstitute.org/cancer/software/GENE-E/index.html) applied to same the data matrix.

Table V – Information about the ^{1}H NMR matrices used for MVA.

Sample type	Aqueous extracts	Lipid extracts
Rows, n samples	95	47
Columns, m variables (intensities)	39391	20973
Spectral interval (ppm)	0.5 – 10	0.5 – 6
Exclusion areas (ppm)	(1.533 – 1.562) (1.915 – 1.925) (2.232 – 2.245) (2.362 – 2.372) (2.729 – 2.737) (3.244 – 3.258) (3.348 – 3.366) (4.634 – 5.00) (7.28 – 7.72)	(1.453, 1.75) (2.15, 2.74) (3.45, 3.51) (5.57, 5.6)
Integration mode	Sum of absolute intensities	

2.3.2. Spectral integration and univariate statistics

To evaluate metabolite quantitative variations, selected signals in the 1D spectrum were integrated using Amix-Viewer (version 3.9.14, BrukerBiospin, Rheinstetten) and normalized by the total spectral area. Spectral integration was performed by calculating the area under a certain signal for which integration limits were manually defined.

Data normality was assessed through the Shapiro test. For normal distributed data, the *t*-test was then applied, and for not normally distributed data, the Wilcoxon test was used. The *p*-value for each metabolite was considered significant when it was lower than 0.05 (confidence level 95 %). Also, for each metabolite, the percentage of variation and respective error were calculated, along with the effect-size (*d*) and respective 95 % confidence interval. The *p*-value and effect-size obtained by the statistical tests allowed the significance and magnitude of the differences between the means of the two classes to be assessed. The resulting data was plotted into a heat map using Matlab 7.14.0.739 (The MathWorks Inc., Massachusetts, USA) to help visualizing the most significant variations.

CHAPTER 3 – Results and Discussion

3.1. Metabolic profile of murine macrophages assessed by ^{1}H NMR spectroscopy

3.1.1. Metabolic composition of murine macrophages (RAW 264.7 cell line): spectral assignment based on 1D and 2D NMR experiments

By reflecting substrate utilization and production within intermediary metabolism, the metabolic composition of cells under different conditions may help assessing the cells' physiopathological status and their response to different stimuli. Here, the basal metabolic composition of murine macrophages (RAW 264.7 cell line) was investigated through the analysis of 1D and 2D ^{1}H NMR spectra of aqueous and lipid cell extracts. Figure 8 shows the standard ^{1}H NMR spectrum of an aqueous extract from RAW 264.7 cells, where a multitude of signals was detected, reflecting the complex sample composition.

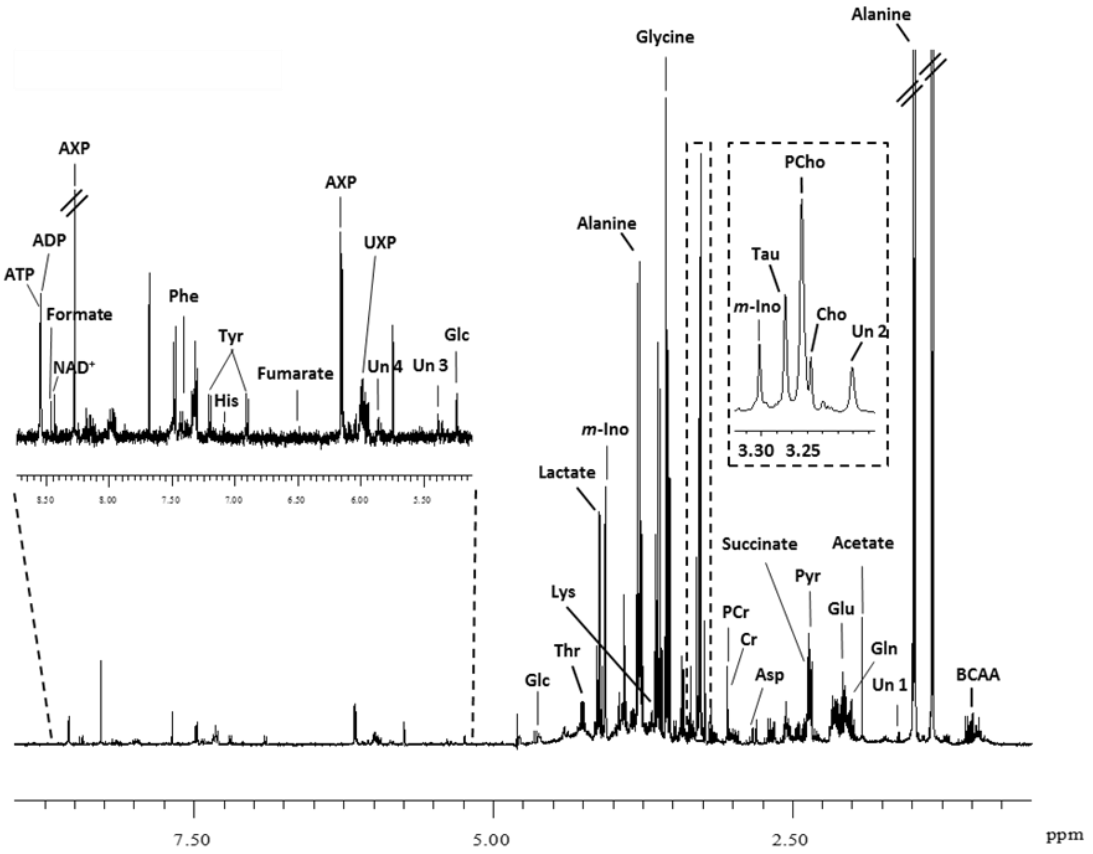

Figure 8 – Representative 500 MHz ^{1}H NMR spectrum of an aqueous extract from RAW 264.7 cells. Some assignments are indicated: three-letter code used for amino acids, ADP adenosine diphosphate, ATP adenosine triphosphate, AXP (ADP/ATP), BCAA branched chain amino acids, Cr creatine, NAD Nicotinamide adenine dinucleotide, PCr phosphocreatine, PCho phosphocholine, Un unassigned, UXP uridine diphosphate/uridine triphosphate (UDP/UTP).

The corresponding 2D spectra are shown in Figure 9. The ^{1}H-^{1}H TOCSY spectrum (Figure 9A) reveals intramolecular spin-spin connectivities, helping to unambiguously identify several compounds with signals overlapped in the 1D spectrum. The ^{1}H-^{13}C HSQC spectrum (Figure 9B) was particularly helpful to identify singlets (without TOCSY cross peaks) or to aid the assignment of cross peaks still overlapped in TOCSY (taking advantage of the larger chemical shift dispersion of ^{13}C resonances). Finally, the *J*– resolved spectrum (Figure 9C) was also useful to distinguish highly overlapped signals and provided information on signal multiplicity. Table VI shows the complete list of compounds identified, along with their ^{1}H and ^{13}C chemical shifts, measured in 1D and 2D NMR spectra.

The low-frequency region (δ 0-3) shows resonances from several amino acids, like branched chain amino acids, alanine and aspartate, but also organic acids like lactate, acetate and pyruvate. In the mid-frequency region (δ 3-5.5), additional intracellular metabolites were detected, including creatine, phosphocreatine, glycine, choline-containing compounds, taurine, *myo*-inositol and threonine. Glucose was also present in the spectrum, however it was found to arise from residual medium not completely washed off the dishes before metabolite extraction. Hence, glucose variations were disregarded since they were not induced by macrophages metabolism. The high-frequency region (δ 5.5-10) is characterized by signals arising from aromatic amino acids (tyrosine and phenylalanine), organic acids (fumarate and formate) but also nucleotides (ADP, ATP, UDP, UTP and NAD^{+}).

In total, over thirty compounds were identified in the cells aqueous extracts, providing significant information on the metabolic composition of RAW 264.7 cells and setting the basis for interpreting the silk nanoparticles' exposure variation discussed ahead.

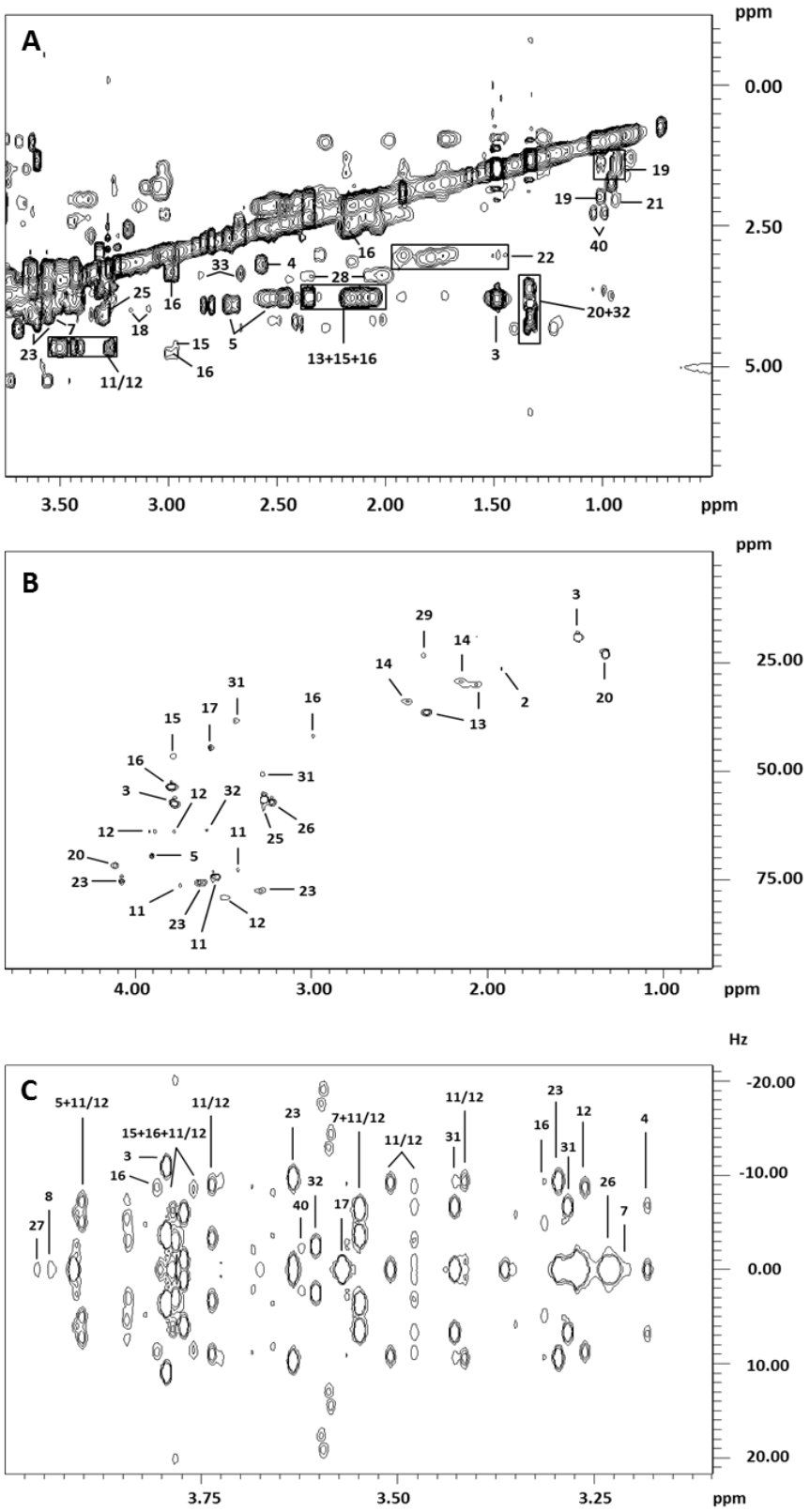

Figure 9 – Expansions of the (A) ^{1}H-^{1}H TOCSY, (B) ^{1}H-^{13}C HSQC and (C) *J*-resolved spectra of aqueous supernatants prepared from murine macrophages (RAW 264.7 cell line). Signals are numbered in accordance with Table VI.

Table VI – Assignment of resonances in the NMR profile of RAW 264.7 aqueous extract of cells (s, singlet; d, doublet; t, triplet; m, multiplet; dd, doublet of doublets).

No.	Compound	δ ^{1}H in ppm (multiplicity, assignment) / δ ^{13}C in ppm
1	Acetate	1.92 (s, β-CH_3)/26.3
2	ADP	4.25 (m, C5'H, ribose); 4.62 (m, C2'H, ribose); 6.16 (d, C1'H, ribose) /89.4; 8.28 (s, C8, ring); 8.54 (s, C2, ring)
3	Alanine	1.49 (d, β-CH_3)/18.9; 3.78 (m, α-CH)/57.2
4	β -Alanine	2.56 (t, β-CH_2); 3.18 (t, α-CH_2)
5	Aspartate	2.69 (dd, β-CH); 2.82 (dd, β'-CH); 3.90 (dd, α-CH)/63.7
6	ATP	4.24 (m, C5'H, ribose); 4.29 (m, C5''H, ribose); 4.41 (m, C4'H, ribose); 4.62 (m, C2'H, ribose); 6.15 (d, C1'H, ribose)/89.4; 8.27 (s, C2, ring); 8.55 (s, NH, ring)
7	Choline	3.22 (s, $N(CH_3)_3$); 3.54 (C**H$_2$**)NH)); 4.07 (m, C**H$_2$**(OH))
8	Creatine	3.04 (s, CH_3); 3.93 (s, CH_2)
9	Formate	8.46 (s, CH)
10	Fumarate	6.52 (s, CH)
11	α-Glucose	3.41 (m, C4H)/72.5; 3.55 (dd, C2H)/74.1; 3.73 (m, C3H)/76.2; 3.83 (m, C6H); 3.85 (m, C5H); 5.24 (d, C1H)
12	β-Glucose	3.26 (dd, C2H); 3.42 (m, C4H)/72.3; 3.47 (m, C5H); 3.49 (t, C3H)/79.0; 3.78 (m, C6H)/63.8; 3.90 (dd C6'H)/63.7; 4.66 (d, C1H)
13	Glutamate	2.06 (m, β-CH)/29.9; 2.13 (m, β'-CH); 2.35 (m, γ-CH_2)/36.4
14	Glutamine	2.14 (m, β-CH_2)/29.6; 2.45 (m, γ-CH_2)/33.8
15	Glutathione, reduced (GSH)	2.17 (m, β-CH2, Glu); 2.56 (m, γ-CH2, Glu); 2.98 (m, β-CH2, Cys);); 3.78 (α-CH)/46.1; 4.57 (m, α-CH2, Cys); 8.37 (NH, Gly); 8.56 (NH, Cys)
16	Glutathione, oxidized (GSSG)	2.17 (m, β-CH2, Glu); 2.56 (m, γ-CH2, Glu); 2.98 (m, β-CH2, Cys)/41.8; 3.31 (m, β-CH2, Cys); 3.78 (α-CH)/53.8; 4.77 (α-CH2, Cys)
17	Glycine	3.56 (s, α-CH_2)/44.5
18	Histidine	3.23 (m, β-CH_2); 7.08 (s, C4H, ring); 7.87 (s, C2H, ring)
19	Isoleucine	0.94 (t, δ-CH_3); 1.01 (d, β'-CH_3); 1.26 (m, γ-CH_2); 1.48 (m, γ'-CH_2); 1.98 (m, β-CH); 3.69 (d, α-CH)
20	Lactate	1.33 (d, β-CH_3)/22.9; 4.12 (m, α-CH)/71.6
21	Leucine	0.96 (d, δ-CH_3); 0.97 (d, δ'-CH_3); 1.70 (m, γ-CH);1.72 (m, β-CH_2); 3.74 (t, α-CH)

No.	Compound	δ ^{1}H in ppm (multiplicity, assignment) / δ ^{13}C in ppm
22	Lysine	1.48 (m, γ-CH_2); 1.73 (m, δ-CH_2); 1.92 (m, β-CH_2); 3.02 (t, ε-CH_2); 3.76 (t, α-CH)
23	Myo-inositol	3.28 (t, C5H)/77.4; 3.54 (C1H, C3H); 3.63 (dd, C4H, C6H)/75.5; 4.07 (t, C2H)/75.2
24	NAD^+	4.23 (m, A5'); 4.36 (m, A4'); 4.39 (m, A4'/N5'); 4.44 (dd, N3'); 4.50 (m, A3'); 4.54 (m, N2'); 6.00 (d, N1'); 6.10 (d, A1'); 8.20 (s, A2); 8.19 (N5); 8.43 (s, A8); 8.83 (d, N4); 9.14 (d, N6); 9.34 (s, N2)
25	Phenylalanine	3.14 (m, β-CH); 3.27 (dd, β'-CH)/56.4; 3.98 (m, α-CH); 7.33 (d, C2H, C6H, ring)/131.9; 7.39 (d, C4H, ring); 7.43 (t, C3H, C5H, ring)
26	Phosphocholine	3.23 (s, $N(CH_3)_3$)/57.0; 3.62 (m, N-CH_2); 4.17 (m, PO_3-CH_2)
27	Phosphocreatine	3.05 (s, CH_3); 3.95 (s, CH_2)
28	Proline	2.00 (m, γ-CH_2); 2.06 (m, β-CH); 2.34 (m, β'-CH); 3.34 (dt, δ-CH); 3.40 (dt, δ'-CH); 4.13 (dd, α-CH)
29	Pyruvate	2.36 (s, β-CH_3)/23.2
30	Succinate	2.40 (s, CH_2)
31	Taurine	3.27 (t, S-CH_2)/50.7; 3.43 (t, N-CH_2)/38.3
32	Threonine	1.34 (d, γ-CH_3); 3.59 (d, α-CH)/63.5; 4.26 (m, β-CH)
33	Tyrosine	3.08 (m, β'-CH); 3.21 (m, β-CH); 3.95 (m, α-CH); 6.91 (d, C3H, C5H, ring); 7.20 (d, C2H, C6H, ring)
34	UDP	4.23 (m, C5'H, ribose); 4.27 (m, C4'H, ribose); 4.40 (t, C2'H, ribose); 4.44 (t, C3'H, ribose); 5.97 (s, C1'H, ribose); 5.98 (d, C6, ring); 7.99 (d, C5, ring)
35	Unassigned (Un.) 1	1.64 (s)
36	Un. 2	3.16 (m)
37	Un. 3	5.38 (m)
38	Un. 4	5.86 (m)
39	UTP	4.27 (m, C5'H, ribose); 4.30 (m, C4'H, ribose); 4.42 (t, C2'H, ribose); 4.45 (t, C3'H, ribose); 5.97 (s, C1'H, ribose); 5.99 (d, C6, ring); 7.99 (d, C5, ring)
40	Valine	0.99 (d, γ-CH_3); 1.05 (d, γ'-CH_3); 2.28 (m, β-CH); 3.62 (d, α-CH)

In regard to lipid extracts, a typical ^{1}H spectrum is shown in Figure 10. This spectrum shows broader signals, compared to that of aqueous extracts, as the larger lipid molecules show faster transverse relaxation (shorter T_2 relaxation time constants, hence larger signal width). Also, there is significant overlap between signals of different lipid species, for instance, it is difficult to distinguish the different fatty acids composing triglycerides or glycerophospholipids. Still, a number of lipid compounds could be distinguished based on specific resonances. Cholesterol and phosphatidylcholine (PTC), two major components of cell membranes, were found to be main contributors to the lipid extract spectrum. Phosphatidylethanolamine (PTE), sphingomyelin (SM) and smaller amounts of neutral lipids (triglycerides and cholesterol esters were also detected). Table VII shows the complete list of lipid compounds identified, along with their ^{1}H and ^{13}C chemical shifts, measured in 1D and 2D NMR spectra (Fig. 11). This assignment is in agreement with the lipid composition previously described for RAW 264.7 cells *(84,85)*.

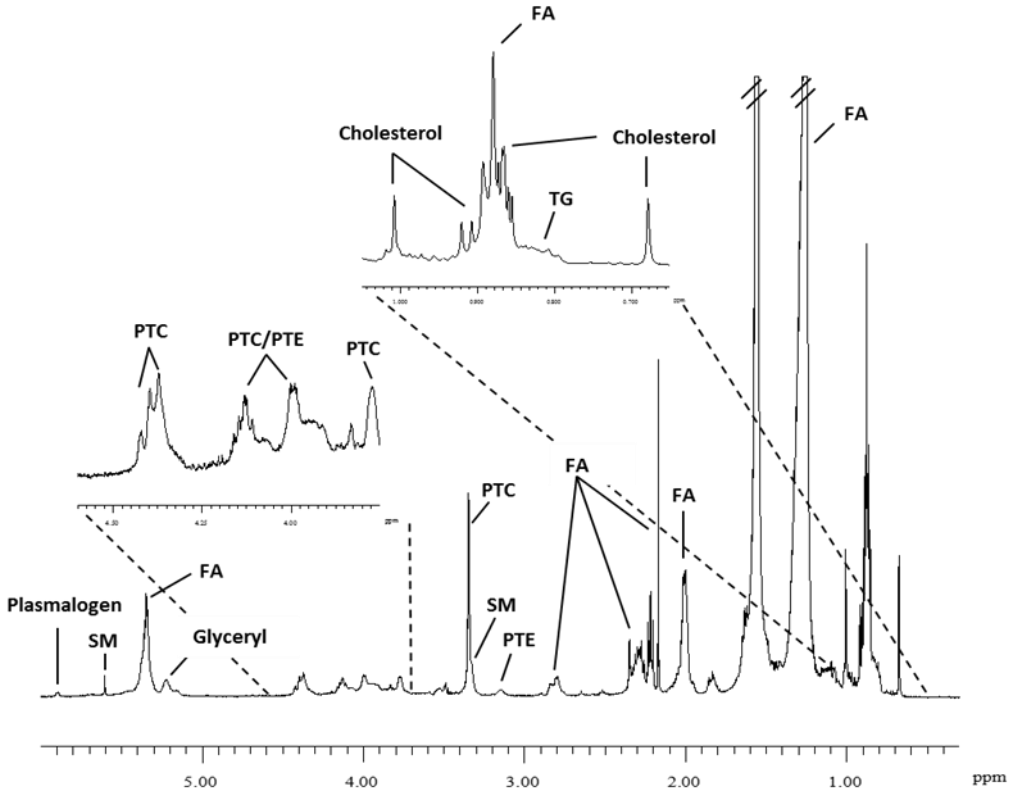

Figure 10 – Representative 500 MHz ^{1}H NMR spectrum of a lipid extract from RAW 264.7 cells. Some assignments are indicated: FA Fatty Acids/Fatty acyl chains, PTC phosphatidylcholine, PTE phosphatidylethanolamine, SM sphingomyelin, TG triglyceride.

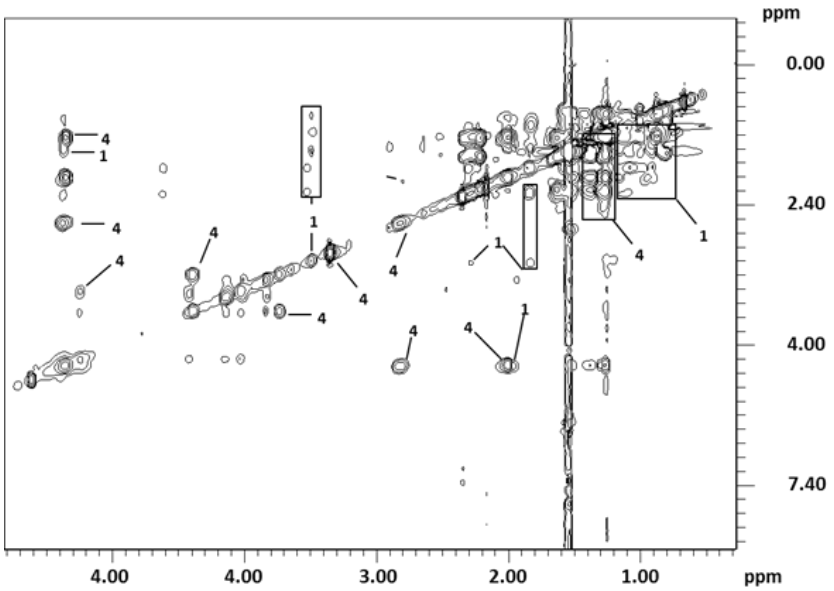

Figure 11 – Expansion of the ^{1}H-^{1}H TOCSY spectrum of a lipid extract prepared from murine macrophages (RAW 264.7 cell line). Signals are numbered in accordance with Table VIII.

Table VII – Assignment of resonances in the NMR profile of RAW 264.7 lipid extract of cells (s, singlet; d, doublet; t, triplet; m, multiplet; dd, doublet of doublets).

No.	Compound	δ ^{1}H in ppm (multiplicity, assignment) / δ ^{13}C in ppm
1	Cholesterol	0.68 (s, CH_3-18)/11.9; 0.86 (d, CH_3-26); 0.87 (d,CH_3-27)/22.4; 0.91 (d, CH_3-21)/18.6; 1.01 (s, CH_3-19)/19.3; 1.05-1.19 (m, multiple protons); 1.26 (d) 1.42-1.55 (m, multiple protons); 1.78-1.87 (m, multiple protons); 1.95-2.02 (m, multiple protons); 2.23/35.9; 2.26 (m, CH_2-4); 3.48-3.55 (m, CH-3); 5.34 (m, CH-6)/122.02
2	Cholesterol ester	1.02 (s, CH_3-19); 1.57 (m, multiple protons); 1.84 (m,CH_2-2); 2.31 (m, CH_2-4); 4.62 (m, CH-3)/48.7
3	Fatty acyl chains (mainly in phospholipids) (FA)	0.88 (t, C**H$_3$**$(CH_2)_n$); 1.25 (m, (CH_2)n)/29.6; 1.25 (m, $(CH_2)_n$)/31.8; 1.55-1.65 (m, -C**H$_2$**-CH_2CO)/27.0; 1.98-2.09 (m, -C**H$_2$**CH=)/27.0; 2.25-2.35 (m,-C**H$_2$**COOR)/21.1; 2.77-2.87 (m, =CHC**H$_2$**CH=)/25.6; 5.35 (m, -**H**C=C**H**-)/130.0

No.	Compound	δ ^{1}H in ppm (multiplicity, assignment) / δ ^{13}C in ppm
4	Phosphatidylcholine (PTC)	0.89/14.1; 1.26-1.37 (multiple protons)/29.5;1.30/22.6; 1.59(s)/24.6; 2.06/27.2; 2.28-2.34 (m)/34.1 ; 2.81 (s); 3.35/54.8 (s, $N(CH_3)3$; 3.73 (CH_2-N)/67.0; 3.95 (Glyceryl CH_2 *sn*3)/63.6; 4.12, 4.38 (Glyceryl CH_2 *sn*1); 4.40 (CH_2-OP); 5.24 (Glyceryl CH *sn*2); 5.35/129.8
5	Phosphatidylethanolamine (PTE)	3.18 (s, CH_2-N); 3.55 (Glyceryl CH_2 *sn*1)/48.8; 3.92 (Glyceryl CH_2 *sn*3); 4.12 (CH_2-OP)/62.7; 5.15 (Glyceryl CH *sn*2)
6	PTE plasmalogen	1.27 ($(CH_2)_n$); 1.99 (-CH=CH-C**H$_2$**); 4.34 (-C**H**=C**H**-); 5.91 (-C**H**=C**H**-)
8	Sphingomyelin (SM)	3.32 (s, $N(CH_3)_3$); 4.40 (-C**H**=C**H**-)/50.4; 5.70 (-C**H**=C**H**-)
9	Triglycerides (TG)	0.82 (t, CH_3); 4.12, 4.28 (Glyceryl CH_2 *sn*1/*sn*3); 5.27 (Glyceryl CH s*n*2)

3.1.2. Time-related changes in control cells

As three time points were considered in this study (24, 48 and 72h), the variations in control cells over culture time were inspected, in order to assess the possible influence of sampling time on the metabolic profile. The visual comparison of average spectra from control aqueous extracts suggests that there are some differences along time in some small metabolites (Fig. 12). Multivariate analysis further confirms this observation, as samples from different time points are reasonably separated in the PCA scores scatter plot along PC1 (Figure 13). By analysing the corresponding loadings (not shown), it becomes clear that while branched chain amino acids, lysine, pyruvate, choline compounds and aromatic amino acids decreased along culture time, alanine, glutamate, creatine, phosphocreatine, *myo*-inositol, glycine, lactate and nucleotides increased. These variations reflect the cells metabolic adaptations during growth and highlight the dynamic nature of the metabolome.

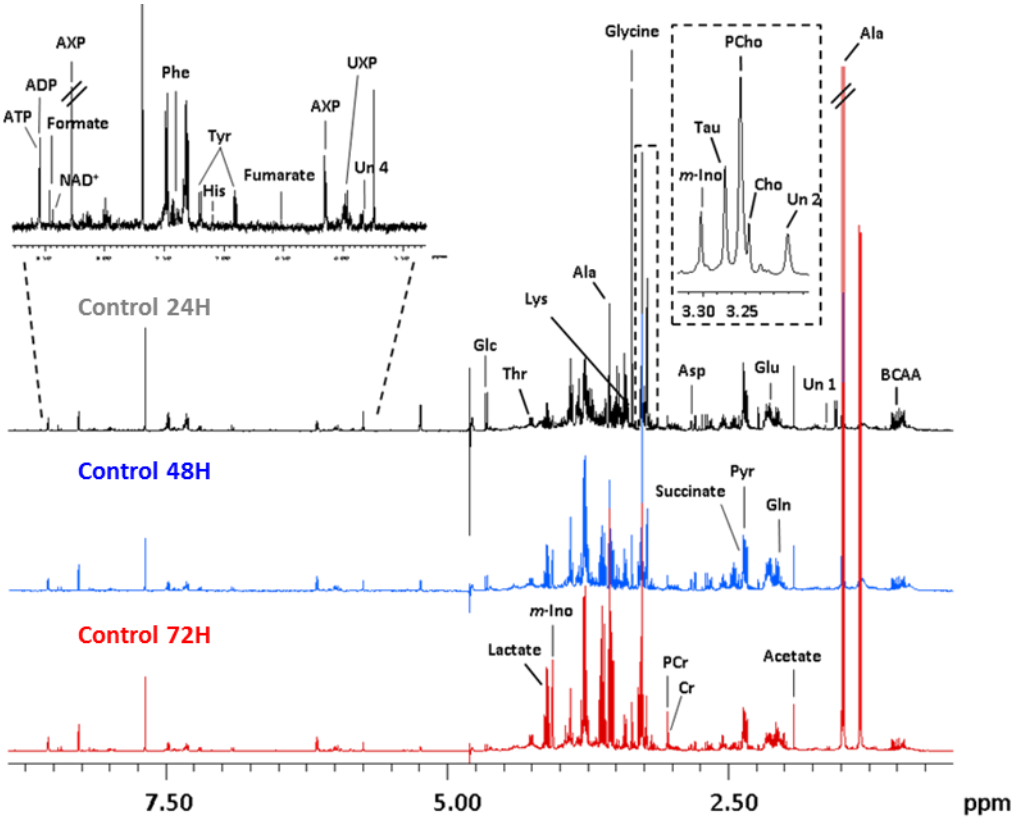

Figure 12 – Average ^{1}H NMR spectra of aqueous extracts of RAW 264.7 cells at 24, 48 and 72 hours.

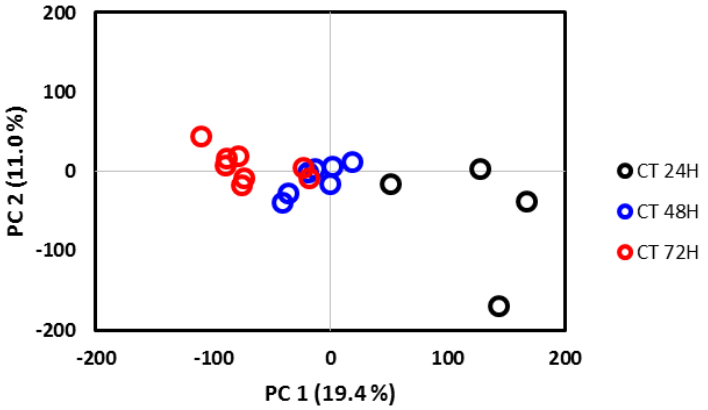

Figure 13 - PC1 vs PC2 scores scatter plot obtained by PCA of ^{1}H NMR spectra from aqueous extracts of control cells collected at different time points.

In regard to lipid extracts, the variations in control cells also revealed the influence of sampling time on the metabolic profile, as seen through both visual comparison of the average spectra (Fig. 14) and multivariate analysis (Fig. 15). By analysing the corresponding loadings (not shown), it becomes clear that while triglycerides, fatty acyl chains, mainly in phospholipids, and sphingomyelin did not show significant differences along culture time, cholesterol, phosphatidylcholine, phosphatidylethanolamine, and plasmalogen increased, possibly reflecting changes in membrane composition during cell growth.

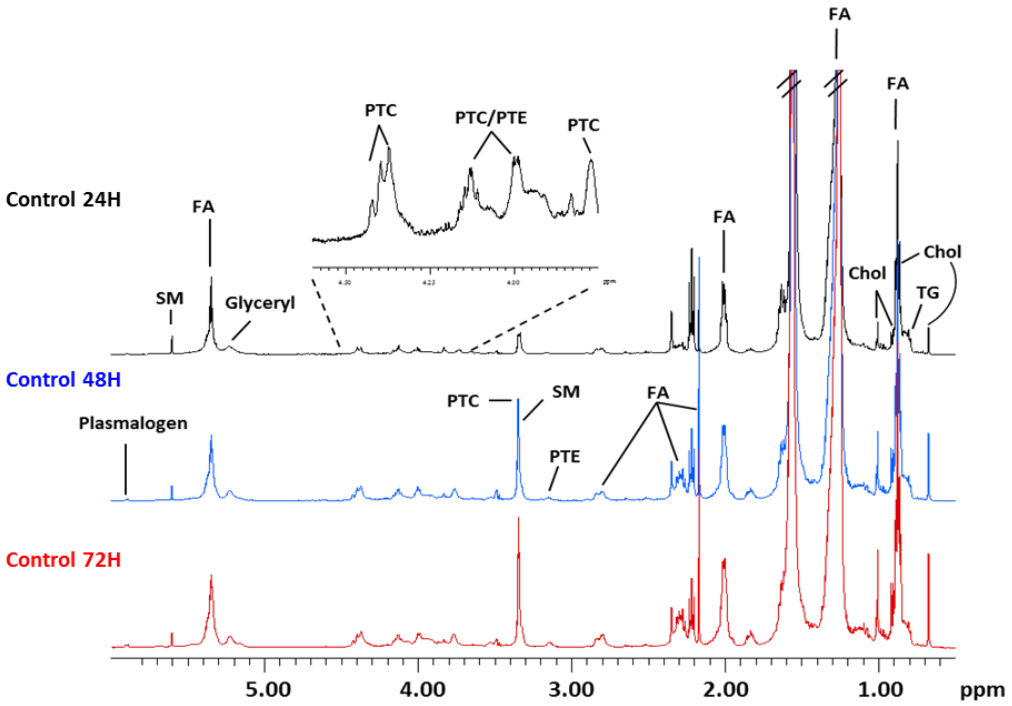

Figure 14 - Average ^{1}H NMR spectra of lipid extracts of RAW 264.7 cells at 24, 48 and 72 hours

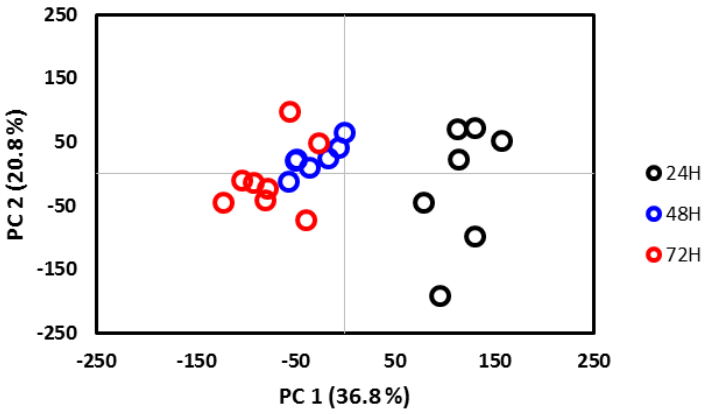

Figure 15 - PC1 vs PC2 scores scatter plot obtained by PCA of ^{1}H NMR spectra from lipid extracts of control cells collected at different time points.

3.2. Impact of silk nanoparticles on macrophage metabolism

3.2.1. Cytotoxicity results

In order to assess the growth characteristics of the RAW cell line and determine the best time range for evaluating the effects of silk nanoparticles (SNPs), a growth curve has been established (Figure 16). The initial cell density plated on each dish was chosen in order to have sufficient cells for metabolomics already at the early time point (24h). The cells were found to reach confluence about day 4 and to be in the exponential growth phase (in which the cell population doubles at a characteristic rate) from 24 to 72h. Thus, this time range was selected for the SNPs exposure studies, as during this phase the cells are more vulnerable to external stimuli. Investigating the cellular response in the first 72 hours exposure also allows to maximize the difference between control and treatment groups and minimize assay artefacts due to confluence.

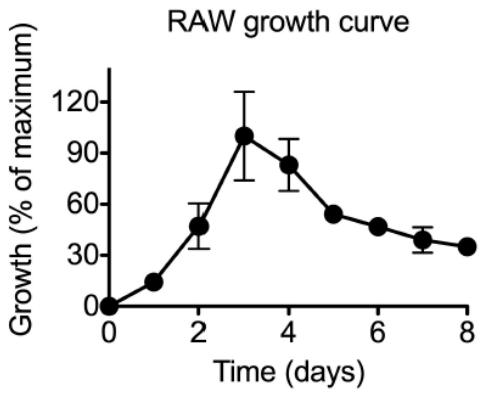

Figure 16 – Growth curve of RAW 264.7 cells. Cells were plated at a density of 1.5×10^4 cells/cm^2 and cell growth was monitored daily. (n=3 independent experiments. Error bars represent standard deviation).

To investigate the effects of silk nanoparticles on cell viability and determine the IC50 value (that indicates the concentration needed to inhibit cell viability by half), RAW cells were exposed to increasing concentrations of SNPs. After 24, 48 and 72 hours of incubation, MTT solution was added to each of the samples and cell viability was assessed, as described in the experimental section.

For 24 and 48h, cell viability did not decrease below 60% across the tested concentration range of silk nanoparticles, with IC50's > 1000 μg/mL at both time points (Figure 17). Curiously, the decrease in cell viability upon exposure to 2.5-50 μg/mL SNPs seemed to be

more abrupt at 24h. At 72h of exposure, cell viability decreased steadily with increasing SNP concentration, reaching about 40% of cell viability for the maximum concentration tested (1000 µg/mL). However, it is possible that cell overgrowth at 72h may also affect cell viability and that the observed decrease does not exclusively arise from SNPs toxicity.

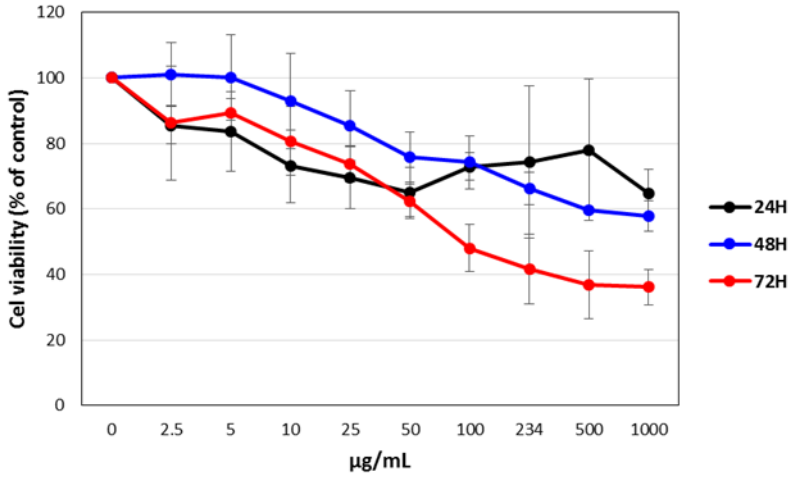

Figure 17 – Cytotoxicity of silk nanoparticles (SNPs) on RAW264.7 cells. Cells were exposed to nanoparticles for 24 h, 48 h or 72 h and cell viability was determined by the MTT assay. (n=4 independent experiments, ± standard error of the mean).

3.2.2. Effects on the metabolome of macrophages assessed by ^{1}H NMR spectroscopy of cellular aqueous extracts

This section presents the variations in the metabolome of RAW 264.7 cells in response to silk nanoparticles (SNPs) when compared to controls and taking into account different factors, such as the concentration and duration of exposure.

Figure 18 shows the average ^{1}H NMR spectra of aqueous extracts from RAW 264.7 cells after 48 hours of exposure to SNPs at low (10 µg/mL) and high (500 µg/mL) concentrations, and their corresponding controls (non-exposed). The visual comparison of the three spectra allowed several differences to be suggested, namely in the levels of branched chain amino acids (BCAA), creatine (Cr), phosphocreatine (PCr), glycine, lactate, formate and tyrosine (increased in exposed cells) and of alanine, aspartate, threonine, *myo*-inositol, and nucleotides (decreased in exposed cells). Additionally, these spectra clearly demonstrate that SNPs caused the metabolome of RAW 264.7 to change in a concentration-dependent manner, with the high concentration causing much stronger effects.

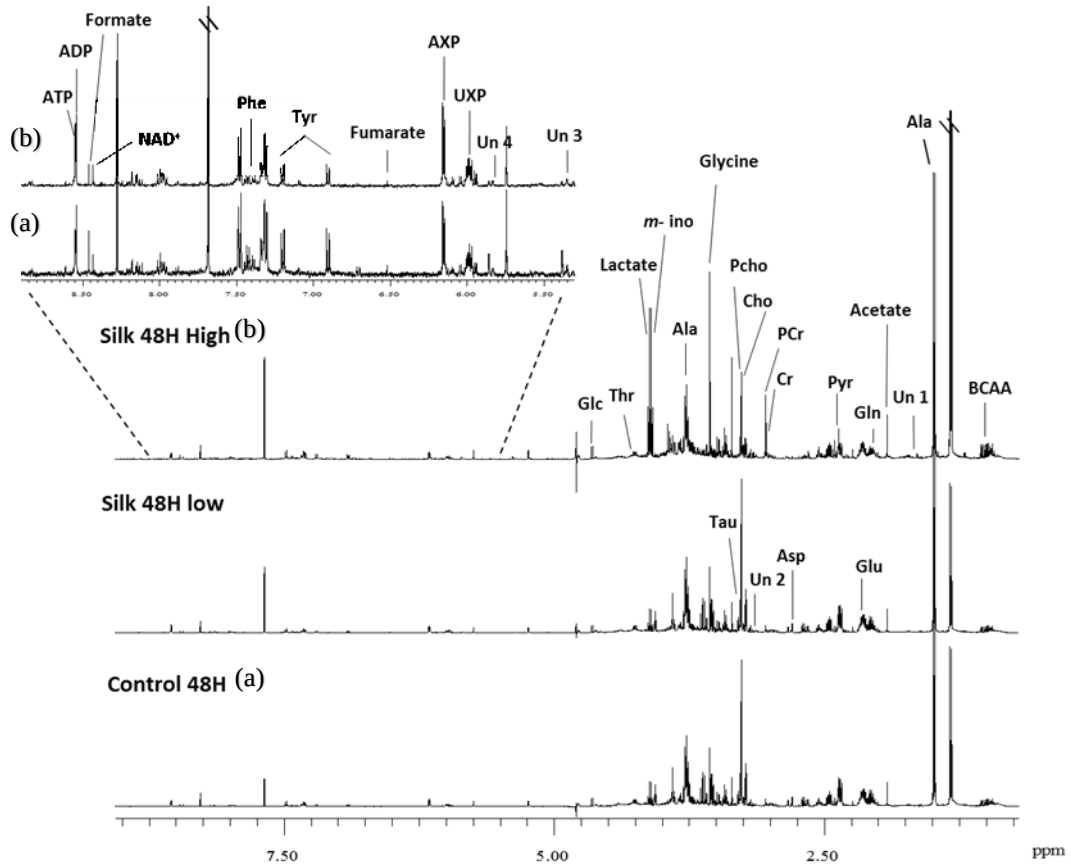

Figure 18 – Average ^{1}H NMR spectra of aqueous extracts of RAW 264.7 cells after 48h exposure to SNPs, with low and high concentration of SNPs.

To evaluate the influence of both SNP concentration and exposure time on the metabolic responses to silk nanoparticles, multivariate analysis was performed. As a first approach to unveil trends and clusters within the samples, unsupervised methods, namely Principal Component Analysis (PCA) and Hierarchical Cluster Analysis (HCA) were applied.

The scores scatter plot resulting from applying PCA to the spectral profiles (Figure 19A) showed a trend for a time- and concentration-dependent response to SNPs. A metabolic similarity between low-concentration groups and controls is displayed at all time-points, while, within each time point, the high-concentration samples tend to be further away. Moreover, there is a trend for separation as a function of time, especially between the 24h and the remaining samples. The dendrogram obtained by HCA (Figure 19B) confirms these trends: a first node separates the samples exposed to high concentration SNPs for 48 and 72h from the remaining samples, whereas further clustering is primarily a function of time.

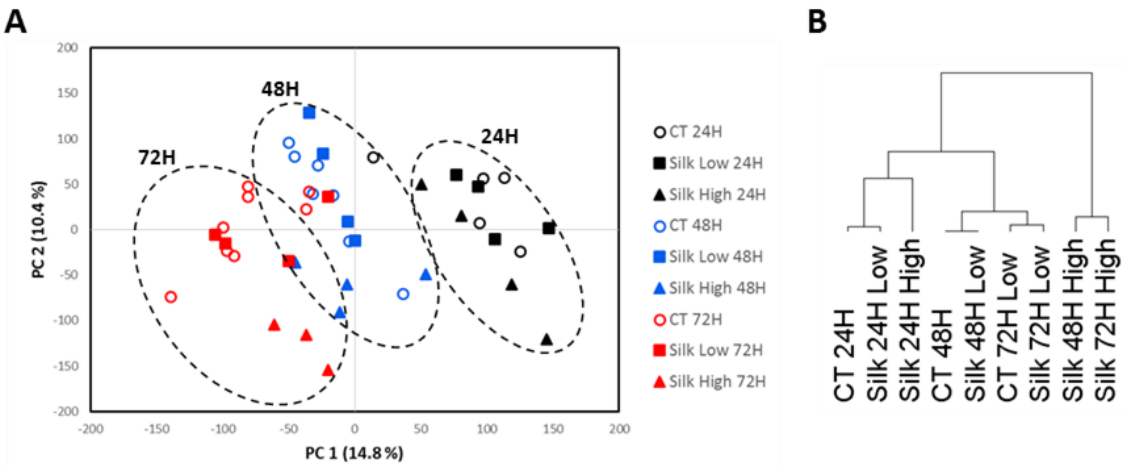

Figure 19 – A) PC1 vs PC2 scores scatter plot obtained by PCA of ^{1}H NMR spectra of cellular aqueous extracts corresponding to control conditions and exposure to SNPs at low (10 µg/mL) and high (500 µg/mL) concentrations, for different time periods (24, 48, 72h) B) Dendrogram obtained by HCA of the same spectral matrix.

Therefore, multivariate analysis was performed considering a sub-set of spectra for each exposure period. The respective PCA and PLS-DA quality parameters (R^2X and R^2Y: explained variance of the X and Y matrices; Q^2: predictive power) are presented in table VIII.

Table VIII – Statistical parameters obtained by PCA and PLS-DA of controls vs SNPs-exposed samples, considering different classes (concentrations and time points).

	PCA	PLS-DA		
MODEL	**R^2X**	**R^2X**	**R^2Y**	**Q^2**
24h: CT vs. SNPs L+H	0.286	0.244	0.987	0.510
48h: CT vs. SNPs L+H	0.333	0.265	0.931	0.198
72h: CT vs. SNPs L+H	0.370	0.300	0.856	0.156
24h: CT vs. SNPs L	0.350	0.284	0.993	0.359
24h: CT vs. SNPs H	0.369	0.329	0.994	0.689
48h: CT vs. SNPs L	0.367	0.311	0.985	0.563
48h: CT vs. SNPs H	0.354	0.343	0.998	0.852
72h: CT vs. SNPs L	0.390	0.267	0.906	-0.025
72h: CT vs. SNPs H	0.437	0.417	0.990	0.907

CT – Control; L – Low concentration (10 µg/mL); H – High concentration (500 µg/mL).

As we can see from this table, the models that best describe the separation between control and NP-exposed samples, i.e. which present higher explained variance and a Q^2 value closer to 1, are the models comparing controls with samples exposed to high concentration SNPs, whereas the models with low concentration SNPs show much lower or even negative Q^2 values. Indeed, the overlap between low concentration SNPs and control samples is visible in the PCA scores plots obtained for each time point (Figure 20, left), while the high-concentration samples were separated. Therefore, only the PLS-DA models built for controls versus high concentration SNPs were considered in further analysis. The corresponding scores show a clear separation between the two classes along LV1 (Figure 20, right), with $Q^2 \geq 0.7$. The respective LV1 loadings (Figure 21), coloured according to variable importance in the projection (VIP), allowed the main compounds responsible for this discrimination to be identified. These plots suggest that some variations are common to all exposure periods, such as the increase in branched chain amino acids, lactate and tyrosine (negative loadings) or the decrease in glutamine, taurine, *myo*-inositol and ATP/ADP (positive loadings), whereas other variations seem to be more time-specific.

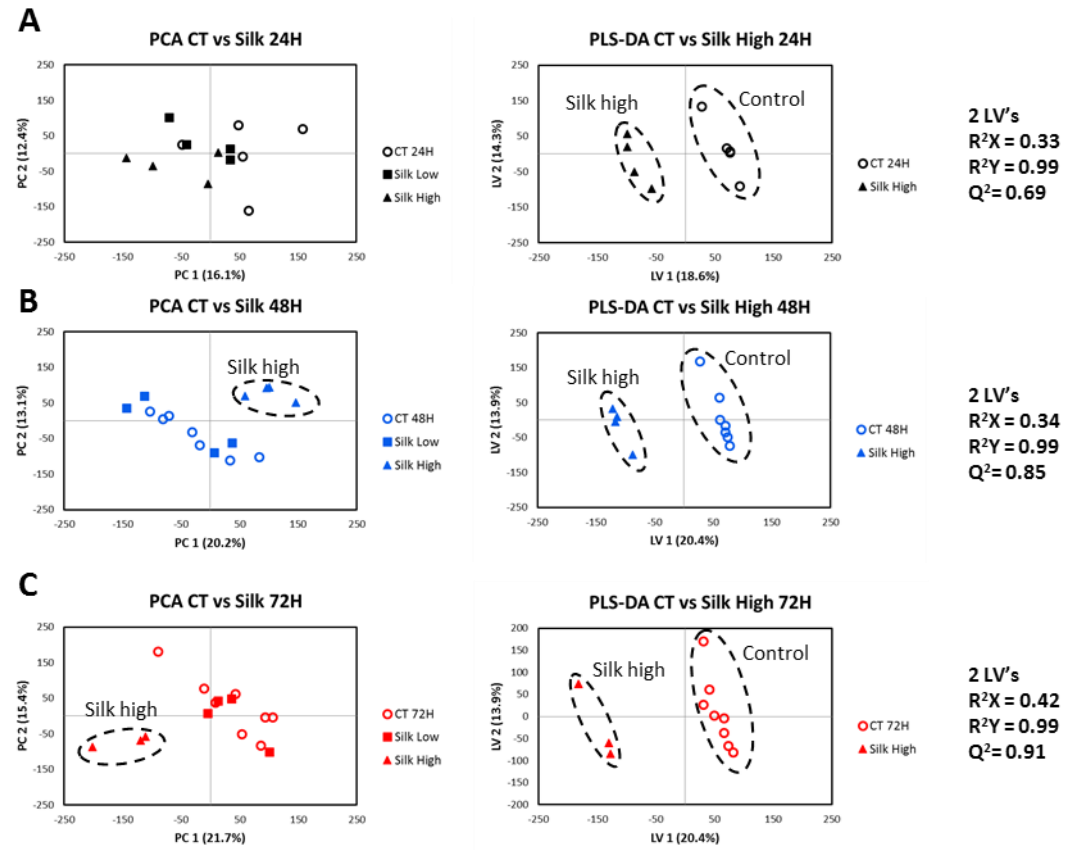

Figure 20 – Scores scatter plots obtained by PCA (left) and PLS-DA (right) of ^{1}H NMR spectra from aqueous extracts of control RAW 264.7 cells and cells exposed to SNPs for (A) 24 hours, (B) 48 hours and (C) 72 hours. Circles, squares and triangles represent controls, low concentration and high concentration of SNPs, respectively.

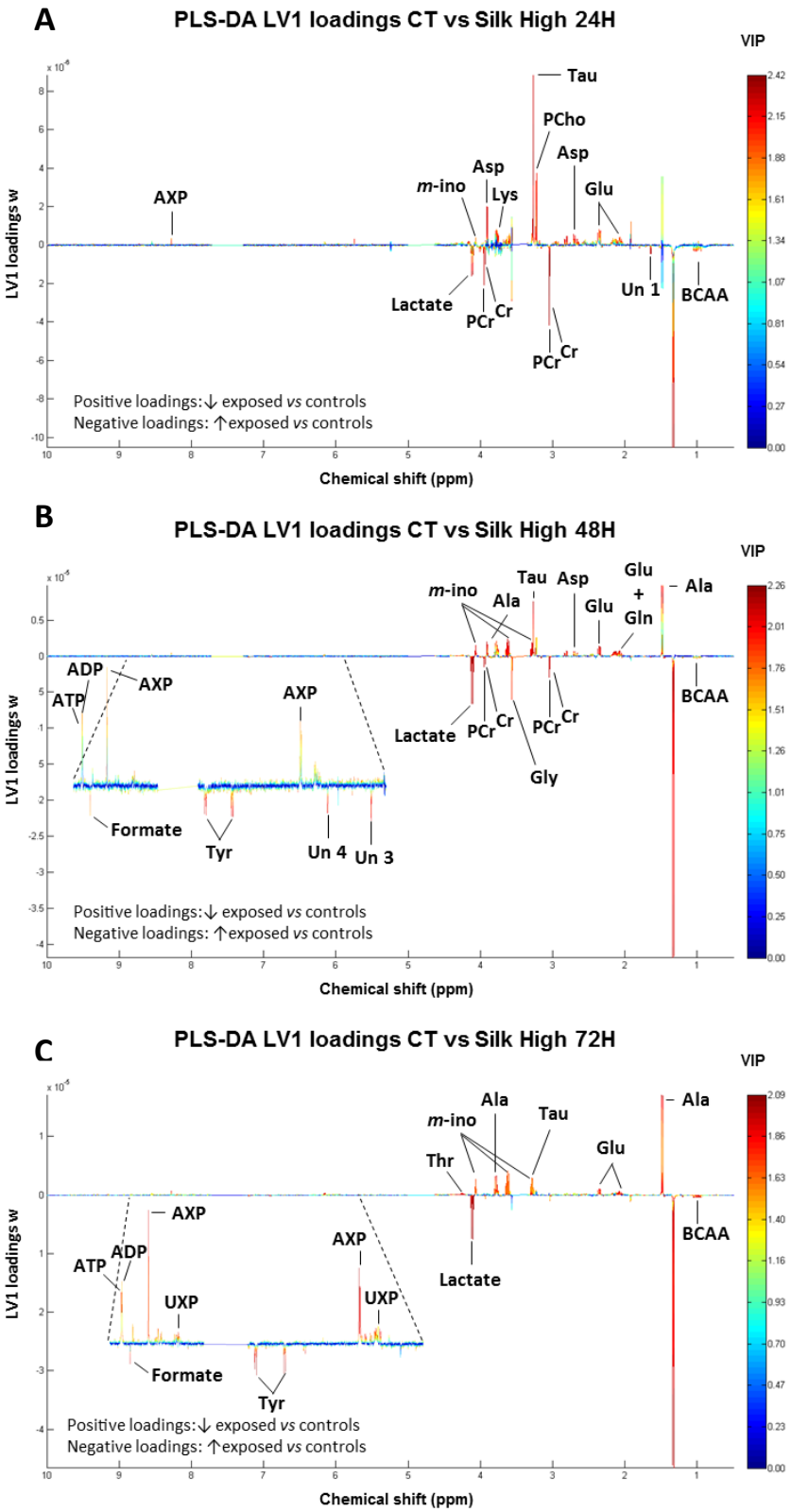

Figure 21 – LV1 loadings *w*, coloured as a function of variable importance in the projection (VIP), corresponding to PLS-DA of ^{1}H NMR spectra from aqueous extracts of control RAW 264.7 cells and cells exposed to SNPs for (A) 24 hours, (B) 48 hours and (C) 72 hours.

For a more thorough analysis of the magnitude and significance of the variations, metabolites with VIP > 1 were integrated in the 1D ^{1}H NMR spectra and the % variation in relation to control cells, as well as the effect size (d) and statistical significance, were calculated for each metabolite. The results for high concentration of SNPs are summarized in Table IX.

Table IX – Metabolite variations in aqueous extracts of RAW 264.7 cells exposed to high concentration (500 µg/mL) of SNPs for 24, 48 and 72 hours, compared to control cells. (s, singlet; d, doublet; t, triplet; m, multiplet; dd, doublet of doublets).

Metabolite (δ/ppm [a], multiplicity)	Silk High 24H		Silk High 48H		Silk High 72H	
	% Var. [b]	*d* [c]	% Var. [b]	*d* [c]	% Var. [b]	*d* [c]
Alanine (d, 1.49)	-	-	-38.02 ± 4.69	-3.96 ± 1.93	-57.60 ± 5.76	-5.21 ± 2.36
Aspartate (dd, 2.82)	-47.16 ± 5.67	-4.49 ± 2.19	-81.37 ± 7.22	-6.48 ± 2.82	-79.15 ± 28.51	-1.48 ± 1.26
Creatine (s, 3.04)	377.57 ± 16.66	7.54 ± 3.35	533.77 ± 19.02	8.39 ± 3.53	163.51 ± 21.16	2.58 ± 1.51
Glutamine (m, 2.35)	-13.89 ± 10.44	-	-28.08 ± 9.45	-1.83 ± 1.33	46.54 ± 31.37	-
Glycine (s, 3.56)	21.16 ± 17.27	-	96.37 ± 18.03	3.31 ± 1.73	20.42 ± 10.85	-
Isoleucine (t, 0.94)	24.12 ± 7.59	1.64 ± 1.32	30.76 ± 6.10	2.64 ± 1.53	78.80 ± 9.20	3.75 ± 1.86
Leucine (d, 0.96)	17.80 ± 7.16	1.25 ± 1.24	38.61 ± 8.70	2.64 ± 1.53	111.35 ± 9.42	4.21 ± 2.01
Lysine (t, 3.02)	34.29 ± 8.98	1.64 ± 1.32	55.09 ± 5.80	4.64 ± 2.16	70.59 ± 8.27	4.79 ± 2.21
Phenylalanine (t, 7.43)	15.21 ± 10.45	-	41.71 ± 8.68	2.59 ± 1.52	57.32 ± 9.65	2.42 ± 1.47
Phosphocreatine (s, 3.05)	392.82 ± 22.18	5.70 ± 2.63	385.89 ± 21.64	6.28 ± 2.75	-	-
Taurine (t, 3.27)	-39.60 ± 6.36	-4.15 ± 2.07	-54.31 ± 5.80	-4.96 ± 2.27	-63.80 ± 11.41	-2.88 ± 1.60
Threonine (m, 4.26)	-	-	-24.11 ± 4.36	-2.96 ± 1.62	-39.60 ± 5.37	-4.43 ± 2.09
Tyrosine (d, 6.91)	23.61 ± 8.82	-	52.98 ± 6.41	4.21 ± 2.02	92.37 ± 9.89	4.79 ± 2.21
Valine (d, 1.05)	26.37 ± 7.30	1.73 ± 1.33	44.91 ± 8.44	3.38 ± 1.75	81.81 ± 10.05	4.32 ± 2.05
Myo-inositol (t, 4.07)	-28.86 ± 12.22	-1.33 ± 1.25	-80.25 ± 9.18	-4.71 ± 2.19	-82.93 ± 16.47	-2.84 ± 1.59
Choline (s, 3.22)	-21.33 ± 13.44	-	-	-	27.55 ± 22.83	-
Phosphocholine (s, 3.23)	-41.93 ± 10.99	-2.75 ± 1.61	-69.73 ± 22.89	-1.75 ± 1.31	-	-
Formate (s, 8.46)	-29.35 ± 16.51	-	48.07 ± 15.27	1.64 ± 1.29	80.63 ± 13.01	3.14 ± 1.67
Fumarate (s, 6.52)	-	-	32.18 ± 21.94	-	-65.55 ± 59.86	-
Lactate (m, 4.12)	84.65 ± 10.22	4.10 ± 2.05	285.09 ± 12.87	9.05 ± 3.79	209.97 ± 19.04	4.79 ± 2.21
Pyruvate (s, 2.36)	-37.42 ± 10.00	-1.88 ± 1.37	-26.38 ± 8.21	-2.03 ± 1.37	-	-
Succinate (s, 2.40)	-23.15 ± 9.89	-	27.36 ± 26.11	-	44.92 ± 14.82	1.52 ± 1.26
ADP (s, 8.54)	-23.65 ± 21.51	-	-29.16 ± 24.59	-	-55.54 ± 13.79	-2.07 ± 1.38
ATP (s, 8.55)	-	-	-43.27 ± 17.77	-1.94 ± 1.35	-52.09 ± 16.07	-2.18 ± 1.41
NAD (s, 8.43)	53.59 ± 36.66	-	-25.92 ± 12.14	-	-50.11 ± 15.35	-1.92 ± 1.35
UXP (s, 5.97)	-	-	-22.63 ± 15.31	-	-30.13 ± 10.44	-1.61 ± 1.28
Un 1 (s, 1.64)	186.40 ± 9.90	5.61 ± 2.60	120.21 ± 12.67	4.45 ± 2.10	48.03 ± 22.85	1.24 ± 1.21
Un 2 (m, 3.16)	39.85 ± 11.69	1.76 ± 1.34	114.96 ± 8.82	5.50 ± 2.46	-	-
Un 3 (m, 5.38)	176.04 ± 45.92	-	204.69 ± 23.11	3.79 ± 1.88	-	-
Un 4 (m, 5.86)	115.74 ± 25.96	2.04 ± 1.41	246.41 ± 22.03	4.70 ± 2.18	-	-

[a] Resonance chosen for signal integration. [b] % Variation. [c] *d* – Effect size in relation to control cells. -, no significant variation.

Fig. 22 shows the heatmap of effect size values representing the magnitude of variation in exposed cells relative to control cells.

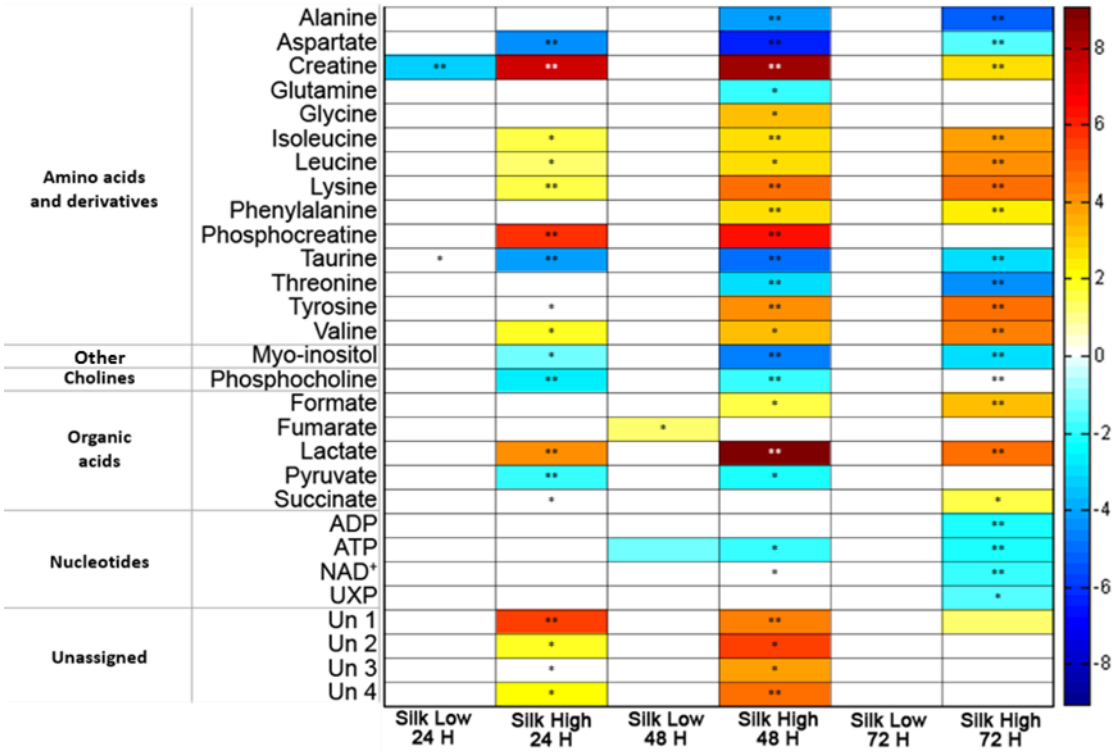

Figure 22 – Heatmap of effect size values of the main aqueous metabolite variations in SNPs-exposed cells (low concentration 10 µg/mL; high concentration 500 µg/mL), at different exposure periods (24, 48 and 72 hours). The colour scale reflects the direction and magnitude of these variations in exposed cells relative to control cells (collected for each respective time point). * $p < 0.05$; ** $p < 0.01$.

As previously noted, the low concentration SNPs induced few changes in the cells metabolome compared to the high concentration SNPs. The time-dependent fluctuations are also visible.

At 24h of exposure, branched chain amino acids, lysine, aromatic amino acids, glycine, lactate, creatine, phosphocreatine, NAD^+ and unassigned signals were higher than in controls, while aspartate, glutamine, cholines, formate, *myo*-inositol, pyruvate, succinate, taurine and ADP were reduced. The profile of the 48h is similar to that of the 24h samples, however a stronger metabolic response was visible for almost all metabolites at this time-point. Also, alanine, threonine, succinate and NAD^+ started to show some decrease in relation to controls (the last one unlike the first time-point), and formate increased. For the 72h period, the metabolic response remains similar to the 48h, although glutamine and choline were found to increase and fumarate to decrease.

3.2.2.1. Proposed biochemical interpretation of nanoparticle-related metabolic changes – aqueous extracts

Several amino acids were found to vary in response to SNPs, in particular, BCAA, lysine, glycine, phenylalanine and tyrosine increased, whereas alanine, aspartate, glutamine, taurine and threonine decreased following SNPs exposure. BCAA are involved in stress, energy and muscle metabolism, being carefully regulated by an enzymatic system. They can undergo different metabolic routes, where valine goes to carbohydrates, leucine to fats and isoleucine to both. Therefore, they can be used for protein synthesis or to form a series of coenzyme A compounds that can be further oxidized for use in the TCA cycle in the forms of acetyl and succinyl CoA. In this work, the energy consumption and protein catabolism could be connected with BCAA increase and mobilization from proteins, but also with the increase of aromatic amino acids (tyrosine and phenylalanine) in response to SNPs exposure *(59,86)*. Threonine can also lead to the formation of acetyl CoA and glycine, and its decrease could be an indicator of that conversion towards glycine, which was found to be increased. Glycine, usually involved in energy release and osmoregulation, is a precursor of reduced glutathione (GSH), an important anti-oxidant that has a key role in maintaining intracellular redox balance for the proper function of cellular proteins. Consistently, another indicator of *de novo* synthesis of GSH is the reduction of glutamine levels at the first 48h of SNPs exposure followed by an increase at the 72 hours. Another indicator is the high consumption of ATP along time, since GSH synthesis depends on ATP-driven enzymatic activity *(87)*. These variations may reflect an adaptive response of RAW 264.7 cells to stress, avoiding oxidative damage *(64,67)*. However, no relevant variations were found directly for GSH or GSSG.

Another indirect regulator of oxidative stress is taurine, which improves mitochondrial function by diminishing superoxide generation. As previously described, the reduction in intracellular taurine levels causes a rise in oxidative stress, usually associated with a decrease in the integrity of the electron transport chain *(88)*. Hence, the decreased levels of taurine induced by SNPs at an early stage indicated that SNPs lead to biochemical and physiological disturbances in many fundamental biological roles, such as anti-oxidation, osmoregulation and membrane stabilization *(64,70)*. Also linked with oxidative phosphorylation in mitochondria is the decrease in ATP production, showing stress-related cellular response induced by SNPs. The reduced ATP levels along time suggests the increase of glycolysis

(77). This is consistent with a significant increase in the levels of lactate coupled with the alteration in succinate and fumarate levels (TCA cycle intermediates), suggesting enhancement of the intracellular anaerobic glycolysis process. Thus, the reduced energy availability leads to an anaerobic metabolism. The glycolytic enzyme, lactate dehydrogenase A (LDHA), which catalyses the conversion between pyruvate and lactate plays an important role in generating lactate, that is expressively elevated *(58,67)*. Alanine can also be converted to pyruvate and it decreased significantly. This perturbation in energy metabolism, accompanied by a decrease in pyruvate indicates a trend in metabolism towards the formation of acetyl CoA and/or lactate *(71)*.

Significant decreases were observed for NAD^+, an important redox coenzyme involved in glycolysis and the TCA of cellular respiration. Depending on the cell metabolic strategy, this coenzyme is found either as an oxidizing (NAD^+) or reducing agent (NADH), used in ATP production and modulating the cellular redox status *(89)*.

Creatine and phosphocreatine, two critical metabolites in the cell's energy shuttle, are highly increased after the SNPs exposure. By reversible interconversion of creatine into phosphocreatine, creatine kinase is the responsible for metabolic regulation of energy fluxes and oxidative phosphorylation. Hence, changes in creatine kinase/phosphocreatine system suggest imbalance in cellular energy homeostasis *(90)*.

Myo-inositol, taurine and choline are metabolites involved is osmo-regulation, therefore their alterations may reflect changes is cellular osmotic balance in the presence of SNPs. *(63,91)*. Moreover, choline and phosphocholine are breakdown products of phosphatidylcholine (PTC), a major cell membrane constituent. Their reduction may be reflective of cell membrane modification and/or proliferation arrest, as these metabolites are important constituents of membrane lipids (whose variations are discussed further ahead) *(58,69)*.

In summary, RAW 264.7 cells' exposure to SNPs resulted in biochemical changes related to energy metabolism and TCA cycle, disturbance of amino acids metabolism and cell membrane modification, comparable to what was previously observed for macrophages exposed to USPIO *(63)* As already mentioned, macrophages are essential cells to recognize, phagocytose, and synthetize inflammatory mediators, being responsible for clearance and trafficking of NPs in vivo. Thus, monitoring macrophages metabolic response to nanoparticles potentially allows to understand the overall physiological response *(92,93)*. In

this work, the metabolome of these cells was indeed found to vary significantly with cell growth and SNP exposure, providing important mechanistic leads on the cell-NP interactions.

3.2.3. Effects on the macrophages' lipidome assessed by ^{1}H NMR spectroscopy of cellular lipid extracts

In order to identify differences in the lipid composition of control cells and cells dosed with both low and high-concentration of SNPs, MVA was applied to the ^{1}H NMR spectra of lipid extracts. As for the aqueous extracts, this analysis was conducted for each exposure period separately. The resulting PCA scores scatter plots are shown in Figure 23 (left). The clearest group separation is seen for the 48h-exposure, where high concentration SNP-exposed samples are well separated from controls and low concentration SNP samples, these two being largely overlapped in the scores map. For the other time points, especially at 72h, group separation is not clear in PCA. Still, PLS-DA was performed for each time point, considering controls vs high concentration SNP-exposed samples. The corresponding PLS-DA scores (Figure 23, right) show a clear separation between the two classes, with $R^2X \geq 0.5$ and a high predictive power ($Q^2 \geq 0.7$).

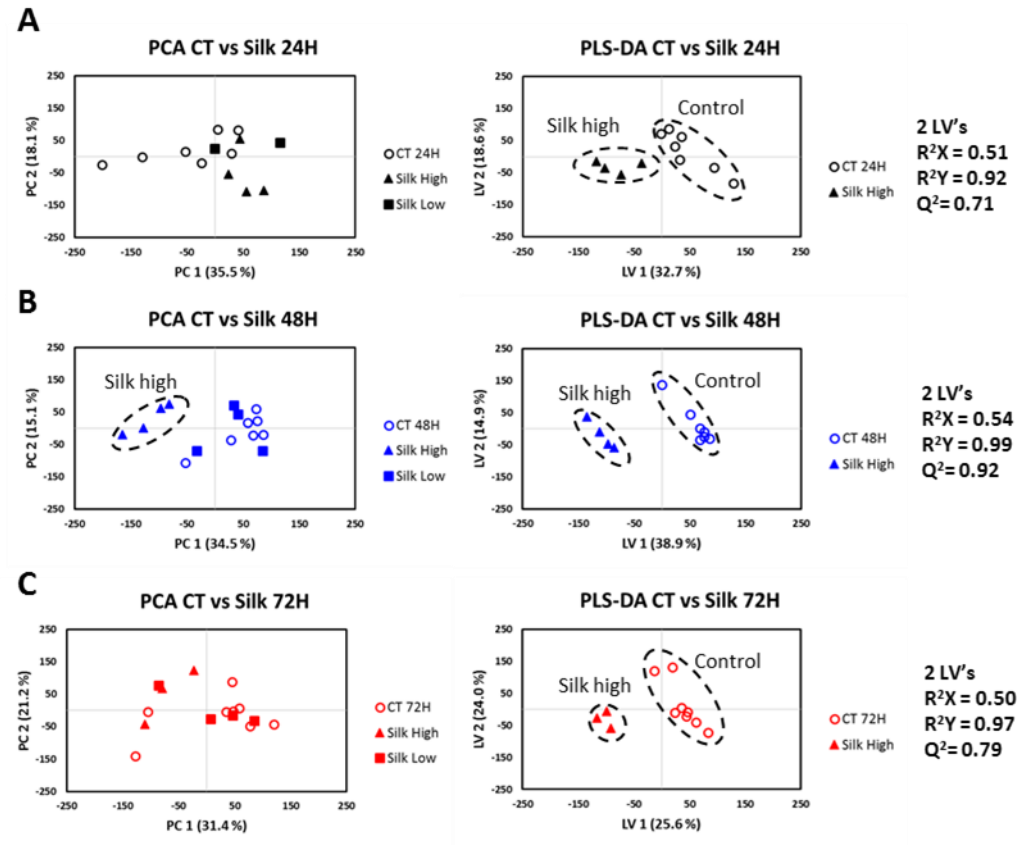

Figure 23 – Scores scatter plots obtained by PCA (left) and PLS-DA (right) of ^{1}H NMR spectra from lipid extracts of control RAW 264.7 cells and cells exposed to SNPs for (A) 24 hours, (B) 48 hours and (C) 72 hours. Circles, squares and triangles represent controls, low concentration and high concentration of SNPs, respectively.

Based on the inspection of LV1 loadings (Figure 24), the main lipid metabolites found to be responsible for the separation between controls and SNP-exposed cells were cholesterol, phosphatidylcholine, phosphatidylethanolamine, sphingomyelin and fatty acyl chains from phospholipids and triglycerides. The response profiles at 24 and 72 hours of exposure were quite similar, and characterised by increases in SM, cholesterol and cholesterol esters (negative loadings) and decreases in the fatty acyl chains of phospholipids (positive loadings) in relation to SNPs exposure. At 48 hours, the exposure to SNPs also led to the decrease of PTE, TG and plasmalogen, and PTC decreased contrarily to the first 24 hours of exposure.

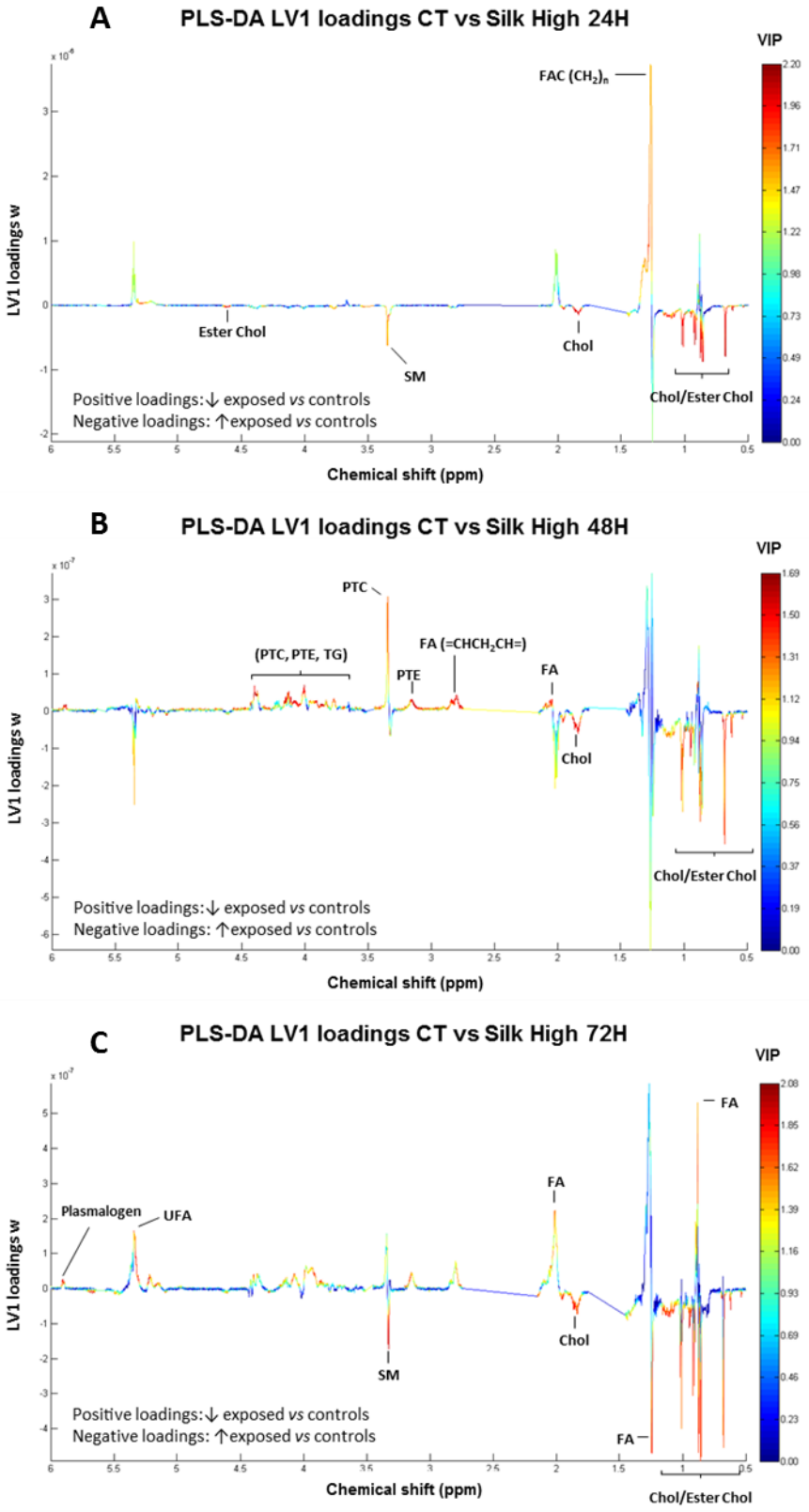

Figure 24 – LV1 loadings w, coloured as a function of variable importance in the projection (VIP), corresponding to PLS-DA of ^{1}H NMR spectra from lipid extracts of control RAW 264.7 cells and cells exposed to SNPs for (A) 24 hours, (B) 48 hours and (C) 72 hours.

The metabolic features discriminating controls and SNP-exposed cells were further inspected by spectral integration of the signals with higher VIP. Those showing statistically significant differences between controls and high concentration SNPs are listed in Table X along with the percentages of variation and effect sizes.

Table X – Metabolite variations in lipid extracts of RAW 264.7 cells exposed to high concentration (500 µg/mL) of SNPs for 24, 48 and 72 hours, compared to control cells. (s, singlet; d, doublet; t, triplet; m, multiplet; dd, doublet of doublets).

Metabolite (δ/ppm [a], multiplicity)	Silk High 24H		Silk High 48H		Silk High 72H	
	% Var. [b]	*d* [c]	% Var. [b]	*d* [c]	% Var. [b]	*d* [c]
Total Chol (s, 0.68)	132.45 ± 11.69	5.09 ± 2.40	38.50 ± 6.19	3.51 ± 1.79	25.29 ± 7.87	1.89 ± 1.34
FA C**H**$_3$(CH$_2$)$_n$ (t, 0.88)	-4.98 ± 0.76	-3.39 ± 1.81	-4.02 ± 1.36	-1.39 ± 1.24	-3.65 ± 1.56	-1.48 ± 1.26
Free Chol (s, 1.01)	65.85 ± 9.28	3.61 ± 1.88	24.91 ± 5.93	2.56 ± 1.51	16.22 ± 7.31	1.46 ± 1.25
Ester Chol (s, 1.02)	114.88 ± 14.43	4.00 ± 2.01	36.06 ± 6.83	2.39 ± 1.46	37.30 ± 8.33	2.14 ± 1.40
FA (CH$_2$)$_n$ (m, 1.25)	6.70 ± 3.68	-	-	-	-	-
FA (-C**H**$_2$CH=) (m, 2.00)	-19.34 ± 10.21	-	-	-	-10.26 ± 3.20	-1.79 ± 1.32
FA (=CHC**H**$_2$CH=) (m,2.83)	8.77 ± 5.96	-	-16.55 ± 4.62	-1.62 ± 1.28	-17.16 ± 5.52	-1.68 ± 1.30
FA (-**H**C=C**H**-) (m, 5.35)	-19.76 ± 9.12	-	-	-	-12.24 ± 4.01	-1.65 ± 1.29
Plasmalogen (5.91)	-	-	-35.25 ± 7.51	-2.46 ± 1.48	-28.80 ± 5.49	-2.88 ± 1.60
PTC (s, 3.35)	45.15 ± 13.53	1.58 ± 1.30	-32.75 ± 22.67	-1.27 ± 1.22	-16.15 ± 5.71	-1.50 ± 1.26
SM (s, 3.35)	372.19 ± 125.38	-	163.23 ± 21.27	2.49 ± 1.49	65.66 ± 22.42	1.26 ± 1.22

[a] Resonance chosen for signal integration. [b] % Variation. [c] *d* – Effect size in relation to control cells. -, no significant variation.

A heatmap representation of the effect size of lipid variations, in exposed cells relatively to controls, is shown in Figure 25.

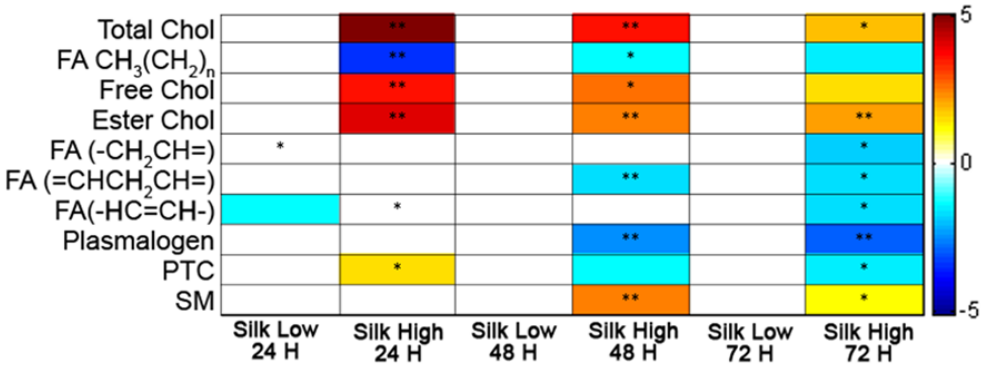

Figure 25 – Heatmap of effect size values of the main lipid metabolite variations in SNPs-exposed cells (low concentration 10 µg/mL; high concentration 500 µg/mL), at different exposure periods (24, 48 and 72 hours). The colour scale reflects the direction and magnitude of these variations in exposed cells relative to control cells (collected for each respective time point). * $p < 0.05$; ** $p < 0.01$. (Chol cholesterol; FA Fatty acyl chains; PTC phosphatidylcholine; SM sphingomyelin).

Cholesterol, cholesterol esters and SM were found to be relatively higher in SNP- exposed samples, whereas FA, plasmalogen and PTC were higher in controls. Interestingly, cholesterol, SM and PTC are components of cell membranes but behave differently along time. These variations are probably associated with cell membrane modification of macrophages, occurring at a later stage (48 hours).

3.2.3.1. Proposed biochemical interpretation of nanoparticle-related metabolic changes – lipid extracts

Lipids have a central role in mammalian cell function, comprising major structural and metabolic components of cells. Lipid metabolism contributes to fulfil energetic needs and membrane fluidity of the cells. This process is very important during macrophage activation and phagocytosis in response to external stimuli, such as nanoparticles' exposure. Also, the ratio of saturated and unsaturated fatty acids can, indeed, modulate macrophage phagocytosis. Therefore, macrophages are capable of alter their lipid profile and produce lipid mediator accordingly to the cell's needs *(85,93)*.

The main changes identified upon SNPs exposure were global increases in cholesterol, cholesterol esters and sphingomyelin, whereas unsaturated fatty acids, plasmalogen and phosphatidylcholine were higher in controls. These changes may reflect variations in

membrane composition and fluidity, similarly to what has been reported for macrophages exposed to silver nanoparticles *(94)*. Moreover, the elevation in cholesterol and sphingomyelin might reflect regulatory cross-talk between cholesterol and sphingolipid metabolism *(85)*. Interestingly, some of these differences were time-dependent, with higher impact at the 48 hours exposure. This may indicate that the first 48 hours were an important period for the phagocytic activity of SNPs by macrophages. As described by Haase's team, the functionality of phagocytic activity is connected with cell membrane integrity *(94)*. Following the 72h time point, metabolites variations seem to stabilize, suggesting some cellular metabolic recovery.

CHAPTER 4 – Conclusions and Prospects

In this work, the metabolic composition of RAW 264.7 cells was characterized by 1D and 2D NMR spectroscopy, which allowed us to establish a database of metabolites for murine macrophages. In the aqueous extract, almost forty metabolites were unambiguously identified, including amino acids, organic acids, choline-containing compounds and nucleotides. Regarding the lipid composition, the assignment of the main lipid classes included cholesterol and cholesterol esters, phosphatidylcholine, phosphatidylethanolamine, sphingomyelin, plasmalogen and fatty acids. Interestingly, the cells metabolome and lipidome were found to change with culture time, reflecting metabolic adaptations during normal cell growth.

The assessment of the compositional changes in macrophages during silk nanoparticles' exposure was also performed. Multivariate analysis was carried out on the NMR spectra, revealing that silk nanoparticles impacted cell metabolism in a time and concentration-dependent manner. While some variations were common to all exposure periods, such as the increase in branched chain amino acids, lactate and tyrosine or the decrease in glutamine, taurine, *myo*-inositol and ATP/ADP, others seemed to be more time-specific. In regard to lipids, cholesterol, cholesterol esters and sphingomyelin were found to be relatively higher in SNP-exposed samples, whereas fatty acids, plasmalogen and phosphatidylcholine were higher in controls.

In summary, RAW 264.7 cells' exposure to silk nanoparticles entailed prominent biochemical changes in cell metabolism, suggesting downregulated TCA cycle activity, energy depletion, disturbance of amino acids metabolism and cell membrane modification.

Particularly, whereas no metabolic changes were observed with the lowest concentration of silk nanoparticles, with cell viability above 70 %, at a higher concentration of SNPs, those changes were clear. Using a high concentration of SNPs, numerous changes were detected and, although cell viability reached a lower value than the IC50 for the 72h period, at the first 48h cell viability remained above 60%. This is a reflex of the ability of macrophages to adapt and reprogram their function in response to compositional changes relatively to growth needs and SNPs-exposure.

A thorough understanding of nanomedicines biological effects will allow an optimization of their rationale design and safety profiles, from early development stages. Metabolic profiling offers a window into the impact of external stimuli (such as a nanomaterial) on

cellular metabolism. Therefore, it has the potential to reveal response markers of efficacy or toxicity, as well as provide biochemical insight into mechanisms of action.

In the future, the confirmation of these results could be accomplished with more sensitive techniques such as mass spectrometry, for instance to analyse lipid composition in more detail, and through the measurement of the expression/activity of specific enzymes to follow the fate of selected substrates. Moreover, the assessment of the metabolic alterations of RAW 264.7 cells found to be associated with SNPs, should be compared with other cell type's responses. Also, studies involving surface-modified and/or drug-loaded SNPs should also be performed to evaluate the ability of silk of acting as a drug delivery system.

References

(1) Fadeel, B. (2014) Handbook of Safety Assessment of Nanomaterials: From Toxicological Testing to Personalized Medicine (Torchilin, V., and Amiji, M., Eds.). CRC Press.

(2) Duncan, R., and Gaspar, R. (2011) Nanomedicine(s) under the microscope. *Mol. Pharm. 8*, 2101–2141.

(3) Svenson, S. (2014) What nanomedicine in the clinic right now really forms nanoparticles? *Wiley Interdiscip. Rev. Nanomed. Nanobiotechnol. 6*, 125–135.

(4) (2005) European Science Foundation's Forward Look on Nanomedicine: An European Medical Research Councils opinion.

(5) Logothetidis, S. (2011) Nanomedicine and Nanobiotechnology. *Wiley Interdiscip. Rev. Nanomedicine Nanobiotechnology* (Logothetidis, S., Ed.). Springer Berlin Heidelberg, Berlin, Heidelberg.

(6) Caruthers, S. D., Wickline, S. a, and Lanza, G. M. (2007) Nanotechnological applications in medicine. *Curr. Opin. Biotechnol. 18*, 26–30.

(7) Nitta, S. K., and Numata, K. (2013) Biopolymer-based nanoparticles for drug/gene delivery and tissue engineering. *Int. J. Mol. Sci. 14*, 1629–1654.

(8) Liu, J., Huang, Y., Kumar, A., Tan, A., Jin, S., Mozhi, A., and Liang, X.-J. (2014) pH-sensitive nano-systems for drug delivery in cancer therapy. *Biotechnol. Adv. 32*, 693–710.

(9) Greish, K. (2010) Enhanced permeability and retention (EPR) effect for anticancer nanomedicine drug targeting. *Methods Mol. Biol. 624*, 25–37.

(10) Seib, F. P., and Kaplan, D. L. (2013) Silk for Drug Delivery Applications: Opportunities and Challenges. *Isr. J. Chem. 53*, 756–766.

(11) Danhier, F., Ansorena, E., Silva, J. M., Coco, R., Le Breton, A., and Préat, V. (2012) PLGA-based nanoparticles: an overview of biomedical applications. *J. Control. Release 161*, 505–522.

(12) Panariti, A., Miserocchi, G., and Rivolta, I. (2012) The effect of nanoparticle uptake on cellular behavior: disrupting or enabling functions? *Nanotechnol. Sci. Appl.* 87–100.

(13) Elzoghby, A. O., Samy, W. M., and Elgindy, N. a. (2012) Protein-based nanocarriers as promising drug and gene delivery systems. *J. Control. Release 161*, 38–49.

(14) Vepari, C., and Kaplan, D. (2007) Silk as a biomaterial. *Prog. Polym. Sci. 32*, 991–1007.

(15) Numata, K., and Kaplan, D. L. (2010) Silk-based delivery systems of bioactive molecules. *Adv. Drug Deliv. Rev. 62*, 1497–1508.

(16) Pritchard, E. M., and Kaplan, D. L. (2011) Silk fibroin biomaterials for controlled release drug delivery. *Expert Opin. Drug Deliv. 8*, 797–811.

(17) Mathur, A., and Gupta, V. (2010) Silk fibroin-derived nanoparticles for biomedical applications. *Nanomedicine 5*, 807–820.

(18) Zhao, Z., Chen, A., Li, Y., Hu, J., Liu, X., Li, J., Zhang, Y., Li, G., and Zheng, Z. (2012) Fabrication of silk fibroin nanoparticles for controlled drug delivery. *J. Nanoparticle Res. 14*, 736–746.

(19) Seib, F. P., Jones, G. T., Rnjak-Kovacina, J., Lin, Y., and Kaplan, D. L. (2013) pH-dependent anticancer drug release from silk nanoparticles. *Adv. Healthc. Mater. 2*, 1606–1611.

(20) Hu, X., Shmelev, K., Sun, L., Gil, E.-S., Park, S.-H., Cebe, P., and Kaplan, D. L. (2011) Regulation of silk material structure by temperature-controlled water vapor annealing. *Biomacromolecules 12*, 1686–1696.

(21) Seib, F. P., and Kaplan, D. L. (2012) Doxorubicin-loaded silk films: drug-silk interactions and in vivo performance in human orthotopic breast cancer. *Biomaterials 33*, 8442–8450.

(22) Seib, F. P., Pritchard, E. M., and Kaplan, D. L. (2013) Self-assembling doxorubicin silk hydrogels for the focal treatment of primary breast cancer. *Adv. Funct. Mater. 23*, 58–65.

(23) Wang, X., Yucel, T., Lu, Q., Hu, X., and Kaplan, D. L. (2010) Silk nanospheres and microspheres from silk/pva blend films for drug delivery. *Biomaterials 31*, 1025–1035.

(24) Kundu, J., Chung, Y.-I., Kim, Y. H., Tae, G., and Kundu, S. C. (2010) Silk fibroin nanoparticles for cellular uptake and control release. *Int. J. Pharm. 388*, 242–250.

(25) Tian, Y., Jiang, X., Chen, X., Shao, Z., and Yang, W. (2014) Doxorubicin-loaded magnetic silk fibroin nanoparticles for targeted therapy of multidrug-resistant cancer. *Adv. Mater. 26*, 7393–7398.

(26) Gupta, V., Aseh, A., Ríos, C. N., Aggarwal, B. B., and Mathur, A. B. (2009) Fabrication and characterization of silk fibroin-derived curcumin nanoparticles for cancer therapy. *Int. J. Nanomedicine 4*, 115–122.

(27) Aillon, K. L., Xie, Y., El-Gendy, N., Berkland, C. J., and Forrest, M. L. (2009) Effects of nanomaterial physicochemical properties on in vivo toxicity. *Adv. Drug Deliv. Rev. 61*, 457–466.

(28) Jones, C., and Grainger, D. (2009) In vitro assessments of nanomaterial toxicity. *Adv. Drug Deliv. Rev. 61*, 438–456.

(29) Klaper, R., Arndt, D., Bozich, J., and Dominguez, G. (2014) Molecular interactions of nanomaterials and organisms: defining biomarkers for toxicity and high-throughput screening using traditional and next-generation sequencing approaches. *Analyst 139*, 882–895.

(30) Kunzmann, A., Andersson, B., Thurnherr, T., Krug, H., Scheynius, A., and Fadeel, B. (2011) Toxicology of engineered nanomaterials: focus on biocompatibility, biodistribution and biodegradation. *Biochim. Biophys. Acta 1810*, 361–373.

(31) Arora, S., Rajwade, J. M., and Paknikar, K. M. (2012) Nanotoxicology and in vitro studies: the need of the hour. *Toxicol. Appl. Pharmacol. 258*, 151–165.

(32) Fischer, H. C., and Chan, W. C. W. (2007) Nanotoxicity: the growing need for in vivo study. *Curr. Opin. Biotechnol. 18*, 565–571.

(33) Semete, B., Booysen, L., Lemmer, Y., Kalombo, L., Katata, L., Verschoor, J., and Swai, H. S. (2010) In vivo evaluation of the biodistribution and safety of PLGA nanoparticles as drug delivery systems. *Nanomedicine 6*, 662–671.

(34) Schnackenberg, L. K., Sun, J., and Beger, R. D. (2012) Nanotoxicity (Reineke, J., Ed.). Humana Press, Totowa, NJ.

(35) Duarte, I. F., Lamego, I., Rocha, C., and Gil, A. M. (2009) NMR metabonomics for mammalian cell metabolism studies. *Bioanalysis 1*, 1597–1614.

(36) Fiehn, O. (2002) Metabolomics - The link between genotypes and phenotypes. *Plant Mol. Biol. 48*, 155–171.

(37) Beckonert, O., Keun, H. C., Ebbels, T. M. D., Bundy, J., Holmes, E., Lindon, J. C., and Nicholson, J. K. (2007) Metabolic profiling, metabolomic and metabonomic procedures for NMR spectroscopy of urine, plasma, serum and tissue extracts. *Nat. Protoc. 2*, 2692–2703.

(38) Duarte, I. F. (2011) Following dynamic biological processes through NMR-based metabonomics: a new tool in nanomedicine? *J. Control. Release 153*, 34–39.

(39) Roessner, U., and Bowne, J. (2009) What is metabolomics all about? *Biotechniques 46*, 363–365.

(40) Lindon, J. C., Nicholson, J. K., and Holmes, E. (2011) The Handbook of Metabonomics and Metabolomics. Elsevier.

(41) Balci, M. (2005) Basic 1H- and 13C-NMR Spectroscopy.

(42) Villas-Boas, S. G., Nielsen, J., Smedsgaard, J., Hansen, M. A. E., and Roessner-Tunali, U. (2007) Metabolome Analysis: An Introduction. John Wiley & Sons.

(43) Jacobsen, N. E. (2007) NMR Spectroscopy Explained: Simplified Theory, Applications and Examples for Organic Chemistry and Structural Biology. John Wiley & Sons.

(44) Araníbar, N., Ott, K.-H., Roongta, V., and Mueller, L. (2006) Metabolomic analysis using optimized NMR and statistical methods. *Anal. Biochem. 355*, 62–70.

(45) Fan, T. W.-M., and Lane, A. N. (2008) Structure-based profiling of metabolites and isotopomers by NMR. *Prog. Nucl. Magn. Reson. Spectrosc. 52*, 69–117.

(46) Miller, J. N., and Miller, J. C. (2010) Statistics and Chemometrics for Analytical Chemistry. Pearson/Prentice Hall.

(47) Trygg, J., Holmes, E., and Lundstedt, T. (2007) Chemometrics in metabonomics. *J. Proteome Res. 6*, 469–479.

(48) Wold, S., Esbensen, K., and Geladi, P. (1987) Principal component analysis. *Chemom. Intell. Lab. Syst. 2*, 37–52.

(49) Zhong, C., Yue, X., and Lei, J. (2015) Visual hierarchical cluster structure: A refined co-association matrix based visual assessment of cluster tendency. *Pattern Recognit. Lett. 59*, 48–55.

(50) Meunier, B., Dumas, E., Piec, I., Béchet, D., Hébraud, M., and Hocquette, J.-F. (2007) Assessment of hierarchical clustering methodologies for proteomic data mining. *J. Proteome Res. 6*, 358–66.

(51) Rosipal, R., and Krämer, N. (2006) Overview and Recent Advances in Partial Least Squares. *TU Berlin, Dep. Comput. Sci. Electr. Eng. 3940*, 34–51.

(52) Nakagawa, S., and Cuthill, I. C. (2007) Effect size, confidence interval and statistical significance: A practical guide for biologists. *Biol. Rev. 82*, 591–605.

(53) Liang, J., Tang, M.-L., and Chan, P. S. (2009) A generalized Shapiro–Wilk statistic for testing high-dimensional normality. *Comput. Stat. Data Anal. 53*, 3883–3891.

(54) Gauthier, T. D., and Hawley, M. E. (2015) Introduction to Environmental Forensics. *Introd. to Environ. Forensics*. Elsevier.

(55) Sullivan, G. M., and Feinn, R. (2012) Using Effect Size-or Why the P Value Is Not Enough. *J. Grad. Med. Educ. 4*, 279–82.

(56) Berben, L., Sereika, S. M., and Engberg, S. (2012) Effect size estimation: methods and examples. *Int. J. Nurs. Stud. 49*, 1039–1047.

(57) Cohen, J. (1988) Statistical Power Analysis for the Behavioral Sciences. L. Erlbaum Associates.

(58) Chen, Q., Xue, Y., and Sun, J. (2013) Kupffer cell-mediated hepatic injury induced by silica nanoparticles in vitro and in vivo. *Int. J. Nanomedicine 8*, 1129–1140.

(59) Huang, S.-M., Zuo, X., Li, J. J., Li, S. F. Y., Bay, B. H., and Ong, C. N. (2012) Metabolomics studies show dose-dependent toxicity induced by SiO(2) nanoparticles in MRC-5 human fetal lung fibroblasts. *Adv. Healthc. Mater. 1*, 779–784.

(60) Feng, J., Li, J., Wu, H., and Chen, Z. (2013) Metabolic responses of HeLa cells to silica nanoparticles by NMR-based metabolomic analyses. *Metabolomics 9*, 874–886.

(61) Shinto, H., Fukasawa, T., Yoshisue, K., Tezuka, M., and Orita, M. (2014) Cell membrane disruption induced by amorphous silica nanoparticles in erythrocytes, lymphocytes, malignant melanocytes, and macrophages. *Adv. Powder Technol. 25*, 1872–1881.

(62) Liberman, A., Mendez, N., Trogler, W. C., and Kummel, A. C. (2014) Synthesis and surface functionalization of silica nanoparticles for nanomedicine. *Surf. Sci. Rep. 69*, 132–158.

(63) Feng, J., Zhao, J., Hao, F., Chen, C., Bhakoo, K., and Tang, H. (2010) NMR-based metabonomic analyses of the effects of ultrasmall superparamagnetic particles of iron oxide (USPIO) on macrophage metabolism. *J. Nanoparticle Res. 13*, 2049–2062.

(64) Feng, J., Liu, H., Bhakoo, K. K., Lu, L., and Chen, Z. (2011) A metabonomic analysis of organ specific response to USPIO administration. *Biomaterials 32*, 6558–6569.

(65) Feng, J., Liu, H., Zhang, L., Bhakoo, K., and Lu, L. (2010) An insight into the metabolic responses of ultra-small superparamagnetic particles of iron oxide using metabonomic analysis of biofluids. *Nanotechnology 21*, 395101.

(66) Sadowski, Z. (2010) Biosynthesis and Application of Silver and Gold Nanoparticles, in *Silver Nanoparticles*, pp 257–277. InTech.

(67) Zhang, L., Wang, L., Hu, Y., Liu, Z., Tian, Y., Wu, X., Zhao, Y., Tang, H., Chen, C., and Wang, Y. (2013) Selective metabolic effects of gold nanorods on normal and cancer cells and their application in anticancer drug screening. *Biomaterials 34*, 7117–7126.

(68) Hadrup, N., Lam, H. R., Loeschner, K., Mortensen, A., Larsen, E. H., and Frandsen, H. (2012) Nanoparticulate silver increases uric acid and allantoin excretion in rats, as identified by metabolomics. *J. Appl. Toxicol. 32*, 929–933.

(69) Li, L., Wu, H., Ji, C., van Gestel, C. A. M., Allen, H. E., and Peijnenburg, W. J. G. M. (2015) A metabolomic study on the responses of daphnia magna exposed to silver nitrate and coated silver nanoparticles. *Ecotoxicol. Environ. Saf. 119*, 66–73.

(70) Bu, Q., Yan, G., Deng, P., Peng, F., Lin, H., Xu, Y., Cao, Z., Zhou, T., Xue, A., Wang, Y., Cen, X., and Zhao, Y.-L. (2010) NMR-based metabonomic study of the sub-acute toxicity of titanium dioxide nanoparticles in rats after oral administration. *Nanotechnology 21*, 125105.

(71) Tucci, P., Porta, G., Agostini, M., Dinsdale, D., Iavicoli, I., Cain, K., Finazzi-Agró, A., Melino, G., and Willis, A. (2013) Metabolic effects of TiO2 nanoparticles, a common component of sunscreens and cosmetics, on human keratinocytes. *Cell Death Dis. 4*, e549.

(72) Whitfield Åslund, M. L., McShane, H., Simpson, M. J., Simpson, A. J., Whalen, J. K., Hendershot, W. H., and Sunahara, G. I. (2012) Earthworm sublethal responses to titanium dioxide nanomaterial in soil detected by ^{1}H NMR metabolomics. *Environ. Sci. Technol. 46*, 1111–1118.

(73) Garcia-Contreras, R., Sugimoto, M., Umemura, N., Kaneko, M., Hatakeyama, Y., Soga, T., Tomita, M., Scougall-Vilchis, R. J., Contreras-Bulnes, R., Nakajima, H., and Sakagami, H. (2015) Alteration of metabolomic profiles by titanium dioxide nanoparticles in human gingivitis model. *Biomaterials 57*, 33–40.

(74) Torchilin, V. P. (2007) Micellar nanocarriers: pharmaceutical perspectives. *Pharm. Res. 24*, 1–16.

(75) Katragadda, U., Fan, W., Wang, Y., Teng, Q., and Tan, C. (2013) Combined delivery of paclitaxel and tanespimycin via micellar nanocarriers: pharmacokinetics, efficacy and metabolomic analysis. *PLoS One 8*, e58619.

(76) Cong, W., Liang, Q., Li, L., Shi, J., Liu, Q., Feng, Y., Wang, Y., and Luo, G. (2012) Metabonomic study on the cumulative cardiotoxicity of a pirarubicin liposome powder. *Talanta 89*, 91–98.

(77) Lei, R., Wu, C., Yang, B., Ma, H., Shi, C., Wang, Q., Wang, Q., Yuan, Y., and Liao, M. (2008) Integrated metabolomic analysis of the nano-sized copper particle-induced hepatotoxicity and nephrotoxicity in rats: a rapid in vivo screening method for nanotoxicity. *Toxicol. Appl. Pharmacol. 232*, 292–301.

(78) Yan, G., Huang, Y., Bu, Q., Lv, L., Deng, P., Zhou, J., Wang, Y., Yang, Y., Liu, Q., Cen, X., and Zhao, Y. (2012) Zinc oxide nanoparticles cause nephrotoxicity and kidney metabolism alterations in rats. *J. Environ. Sci. Health. A. Tox. Hazard. Subst. Environ. Eng. 47*, 577–588.

(79) Vega-Villa, K. R., Takemoto, J. K., Yáñez, J. a, Remsberg, C. M., Forrest, M. L., and Davies, N. M. (2008) Clinical toxicities of nanocarrier systems. *Adv. Drug Deliv. Rev. 60*, 929–938.

(80) Herd, H. L., Malugin, A., and Ghandehari, H. (2011) Silica nanoconstruct cellular toleration threshold in vitro. *J. Control. Release 153*, 40–48.

(81) Mosmann, T. (1983) Rapid colorimetric assay for cellular growth and survival: Application to proliferation and cytotoxicity assays. *J. Immunol. Methods 65*, 55–63.

(82) Teng, Q., Huang, W., Collette, T. W., Ekman, D. R., and Tan, C. (2008) A direct cell quenching method for cell-culture based metabolomics. *Metabolomics 5*, 199–208.

(83) Llorach-Asunción, R., Jauregui, O., Urpi-Sarda, M., and Andres-Lacueva, C. (2010) Methodological aspects for metabolome visualization and characterization: a metabolomic evaluation of the 24 h evolution of human urine after cocoa powder consumption. *J. Pharm. Biomed. Anal. 51*, 373–81.

(84) Zoeller, R. a., Wightman, P. D., Anderson, M. S., and Raetz, C. R. (1987) Accumulation of lysophosphatidylinositol in RAW 264.7 macrophage tumor cells stimulated by lipid A precursors. *J. Biol. Chem. 262*, 17212–17220.

(85) Dennis, E. A., Deems, R. A., Harkewicz, R., Quehenberger, O., Brown, H. A., Milne, S. B., Myers, D. S., Glass, C. K., Hardiman, G., Reichart, D., Merrill, A. H., Sullards, M. C., Wang, E., Murphy, R. C., Raetz, C.

R. H., Garrett, T. A., Guan, Z., Ryan, A. C., Russell, D. W., McDonald, J. G., Thompson, B. M., Shaw, W. A., Sud, M., Zhao, Y., Gupta, S., Maurya, M. R., Fahy, E., and Subramaniam, S. (2010) A mouse macrophage lipidome. *J. Biol. Chem. 285*, 39976–39985.

(86) O'Connell, T. M. (2013) The complex role of branched chain amino acids in diabetes and cancer. *Metabolites 3*, 931–945.

(87) Parpura, V., Schousboe, A., and Verkhratsky, A. (2014) Glutamate and ATP at the Interface of Metabolism and Signaling in the Brain. Springer.

(88) Jong, C. J., Azuma, J., and Schaffer, S. (2011) Mechanism underlying the antioxidant activity of taurine: prevention of mitochondrial oxidant production. *Amino Acids 42*, 2223–2232.

(89) Ruggieri, S., Orsomando, G., Sorci, L., and Raffaelli, N. (2015) Regulation of NAD biosynthetic enzymes modulates NAD-sensing processes to shape mammalian cell physiology under varying biological cues. *Biochim. Biophys. Acta - Proteins Proteomics* DOI: 10.1016/j.bbapap.2015.02.021.

(90) Wallimann, T., Tokarska-Schlattner, M., and Schlattner, U. (2011) The creatine kinase system and pleiotropic effects of creatine. *Amino Acids 40*, 1271–1296.

(91) Workman, P., Aboagye, E. O., Chung, Y.-L., Griffiths, J. R., Hart, R., Leach, M. O., Maxwell, R. J., McSheehy, P. M. J., Price, P. M., and Zweit, J. (2006) Minimally invasive pharmacokinetic and pharmacodynamic technologies in hypothesis-testing clinical trials of innovative therapies. *J. Natl. Cancer Inst. 98*, 580–598.

(92) Herd, H. L., Bartlett, K. T., Gustafson, J. a., McGill, L. D., and Ghandehari, H. (2015) Macrophage silica nanoparticle response is phenotypically dependent. *Biomaterials 53*, 574–582.

(93) Biswas, S. K., and Mantovani, A. (2012) Orchestration of metabolism by macrophages. *Cell Metab. 15*, 432–437.

(94) Haase, A., Arlinghaus, H. F., Tentschert, J., Jungnickel, H., Graf, P., Mantion, A., Draude, F., Galla, S., Plendl, J., Goetz, M. E., Masic, A., Meier, W., Thünemann, A. F., Taubert, A., and Luch, A. (2011) Application of Laser Postionization Secondary Neutral Mass Spectrometry/Time-of-Flight Secondary Ion Mass Spectrometry in Nanotoxicology: Visualization of Nanosilver in Human Macrophages and Cellular Responses. *ACS Nano 5*, 3059–3068.

(95) Del Chierico, F., Gnani, D., Vernocchi, P., Petrucca, A., Alisi, A., Dallapiccola, B., Nobili, V., and Lorenza, P. (2014) Meta-omic platforms to assist in the understanding of NAFLD gut microbiota alterations: tools and applications. *Int. J. Mol. Sci. 15*, 684–711.